Structural characterization of naturally fractured geothermal reservoirs in the central Upper Rhine Graben

Carole Glaas, Jeanne Vidal, Albert Genter

Journal of Structural Geology 148 (2021) 104370

Contents lists available at ScienceDirect

Journal of Structural Geology

journal homepage: www.elsevier.com/locate/jsg

Structural characterization of naturally fractured geothermal reservoirs in the central Upper Rhine Graben

Carole Glaas [a,b,*], Jeanne Vidal [c], Albert Genter [a]

[a] 5, rue André Marie Ampère, 67450 Mundolsheim, France
[b] UMR 7516 IPGS, University of Strasbourg, CNRS, 5 Rue René Descartes, 67084, Strasbourg, Cedex, France
[c] University of Chile, FCFM, Department of Geology, Andean Geothermal Center of Excellence (CEGA), Plaza Ercilla 803, Santiago, Chile

ARTICLE INFO

Keywords:
Geothermal reservoir
Natural fractures
Hard rocks
Borehole images
Rhine graben

ABSTRACT

Image logs and the continuous coring of 8 geothermal wells in the Central Upper Rhine Graben (URG) are used for the structural characterization of 3 geothermal reservoirs at Soultz-sous-Forêts, Rittershoffen and Illkirch (France). The naturally permeable fracture zones (FZs) of the hard rocks are the targets of these wells. Subvertical natural fracture networks are striking NNW-SSE to N–S in the granite (inherited from the late-Variscan orogeny) and N–S/NNE-SSW in the sediments (mainly inherited from the Cenozoic era). The permeable fractures in the granite are subparallel to the main striking values. The fracture densities and thicknesses are the greatest in the first 500–1000 m of the granite. The fracture thickness surely reflects the intensity of the paleocirculations. The fracture distribution is governed by power laws and negative exponential laws. However, there is no simple relationship between those fracture properties and the present-day fracture permeability. The permeability is related to multiscale fracture networks channelling the fluids. Large-scale fractures within normal fault zones could be a more promising target than wide networks of distributed small-scale fractures affecting the whole granitic batholith. The geometry between the well trajectory and the fracture network, impacts also significantly the resulting permeability.

1. Introduction

To be economically viable, geothermal projects need to reach a geothermal resource with a heat source, circulating fluids and permeable pathways at a drillable depth. In crystalline rocks with low porosity, permeability is mainly supported by a network of natural fractures (Caine et al., 1996; Faulkner et al., 2010). Fluid is circulated through fracture zones (FZ), which are made of a fault core and damage zones (Caine et al., 1996). The fluid circulation can be enhanced by the presence of active and tensile stresses, normal faults, fracture propagation strike-slip faults and fractures associated with hot springs (Barton et al., 1995; Curewitz and Karson, 1997; Gudmundsson et al., 2002; Faulds et al., 2011; Mitchell and Faulkner, 2012). The occurrence of hydrothermal alteration could contribute to the fluid circulation due to residual channelling occurring inside secondary mineralization, such as automorphic quartz creating incomplete clogging in the FZ core. Hydrothermal alteration could also contribute through the dissolving of primary minerals, which creates some residual porosity in the nearby FZ damage zone (Ledésert et al., 1999). Conversely, fluid circulation in the FZ can be decreased by hydrothermal alteration in the case of secondary clay minerals precipitation, which can clog the fracture network (Ledésert et al., 1999).

In Europe, the geothermal development occurring in the last 30 years in the naturally fractured reservoirs of the Upper Rhine Graben (URG) has proven the existence of a resource that is mainly located at the base of the Triassic sedimentary unit and the top of the Palaeozoic basement that has industrial hydraulic yields (with a range of approximately 3 L/s/bar) and appropriate temperatures (>150 °C) to produce electricity (3 MWe) and/or heat (25 MWth) (Baumgärtner and Lersch, 2013; Baria et al., 2016; Baujard et al., 2017; Vidal and Genter, 2018; Reinecker et al., 2019). More recently, industrial interest in exploiting the lithium concentrations of the geothermal fluid circulating in the fracture network of the URG has increased. The knowledge and characterization of this fracture network are of primary importance to exploit geothermal crystalline fractured reservoirs. The experience has shown that pure hydrothermal concepts lead to the most successful projects (Baujard et al., 2017). Ideally, they do not need Enhanced Geothermal Systems (EGS) technologies, which represent an extra cost and often lead to a loss

* Corresponding author. 5, rue André Marie Ampère, 67450 Mundolsheim, France.
E-mail address: cglaas@unistra.fr (C. Glaas).

https://doi.org/10.1016/j.jsg.2021.104370
Received 18 August 2020; Received in revised form 15 March 2021; Accepted 3 May 2021
Available online 12 May 2021

of public acceptance because of the risk of generating induced seismicity (Häring et al., 2008; Evans et al., 2012).

Generally, fracture networks are studied from relevant outcrops (Brogi, 2008; Bauer et al., 2015). In this paper, we have the opportunity to compare structural data from 3 geothermal sites of the URG, including 8 deep geothermal wells, to understand if there is a structural predisposition to permeability.

More precisely, the aim of this study is to determine how the geometry, scaling law and hydrothermal filling impact the permeability of the reservoir. The studied sites are in the French part of the URG, i.e., Soultz-sous-Forêts and Rittershoffen, which have been exploiting the natural brine since 2016, and the Illkirch site, which is under exploration by drilling and is still under development. The old and new image log and core data come from 8 geothermal wells that intersect the fracture network in the Muschelkalk limestone, the Buntsandstein sandstone and the granitic Palaeozoic basement. The goal is to identify the unvarying and varying structural properties of the multi-scale fracture networks encountered in the studied wells, including the fracture orientation, density, spacing, thickness and permeability indicators. This high-quality dataset will allow for a better understanding of the ideal geothermal target from the structural point of view in the URG or, more generally, in the European Cenozoic Rift System.

2. Structural development of the URG

The URG extends from Frankfurt to Basel, with a maximal width of 30–40 km. It is surrounded by the Vosges mountains forming its western horst and the Black Forest mountains forming its eastern horst, both separated from the graben by local normal faults (Fig. 1a). These domains belong to the same Saxothuringian unit (Edel and Schulmann, 2009). On both horsts, the basement is outcropping, whereas it is hidden by a thick sedimentary cover within the graben. Thermal anomalies are localized along the normal faults, which are interpreted as thermal convection cells along the faults (Schellschmidt and Clauser, 1996; Pribnow and Schellschmidt, 2000; Baillieux et al., 2013). However, the history of the graben is more complex, and this part presents the main steps of its structural evolution, with a focus on its structural inheritance.

2.1. Variscan cycle

The Variscan cycle is characterized by the intrusion of carboniferous

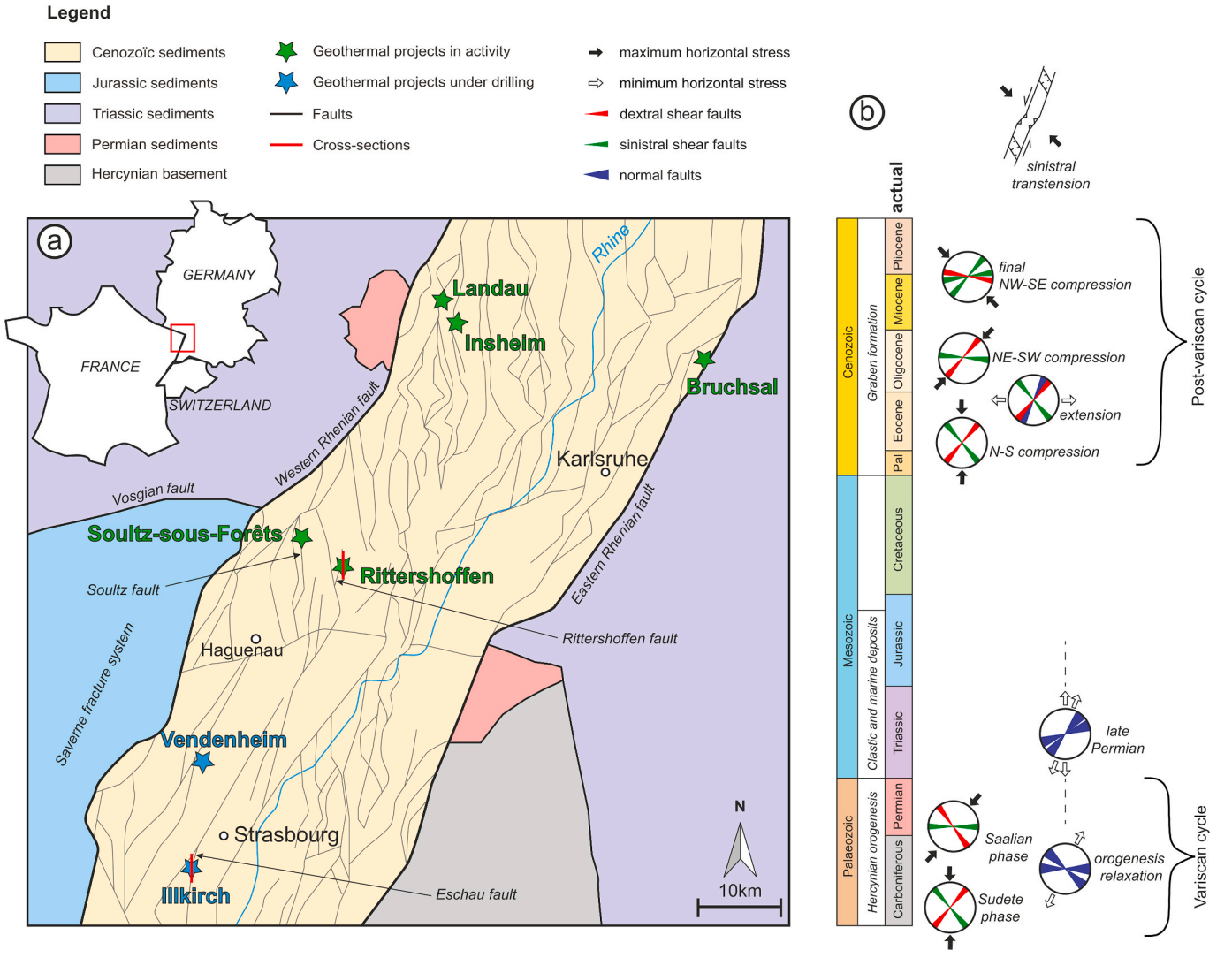

Fig. 1. a) Structural map of the centre of the Upper Rhine Graben showing the faults at the surface from the geoportal GeOrg (2017) in which the faults are derived from 2D vintage seismic data acquired in the Tertiary sediments for oil industry. The locations of the geothermal power plants under exploitation and under drilling are also shown. Two cross sections in reference to Figs. 4 and 5 are represented on the map. b) The orientations of faults and stresses in the URG during the several tectonic phases are presented along the geological timescale from the Palaeozoic to the Cenozoic ages.

granitoïds throughout the crystalline basement from the Visean (340 Ma) and the Permian (270 Ma) eras. These granitoïds were emplaced following a NE to NNE axis along the main weak zones, such as collisional or shear zones (Lagarde et al., 1992; Altherr et al., 1999, 2000; Edel and Schulmann, 2009). The Variscan cycle is also characterized by several tectonic phases (Fig. 1b). The Sudete phase is the structuration of the orogenesis and consists of a N–S compression generating sinistral NE-SW and dextral NW-SE shear faults (Fig. 1b). Then, an extension along an NNE-SSW axis is observed, which reactivates the normal faults oriented NW-SE to WNW-ESE until the Permian. The Saalian phase is marked by compression and thrusts in the NE-SW direction, which are associated with sinistral NW-SE and dextral E-W shear faults (Burg et al., 1984). The end of the Permian is characterized by a N–S to NNE-SSW extension that forms the Permian basin along faults oriented NE-SW to ENE-WSW (Villemin and Bergerat, 1987; Schumacher, 2002; Ziegler et al., 2006).

2.2. Post-variscan cycle

The extension observed at the late Permian continued until the Jurassic in some parts of the URG, inducing fluid migrations and several mineralization events (Clauer et al., 2008; Bossennec et al., 2020). The Cenozoic rifting affects the Variscan basement but also the sediments of the Buntsandstein, the Muschelkalk and the Jurassic. Villemin and Bergerat (1987) and Schumacher (2002) propose a model in 4 tectonic phases (Fig. 1b). First, at the early Eocene, a N–S compression under the

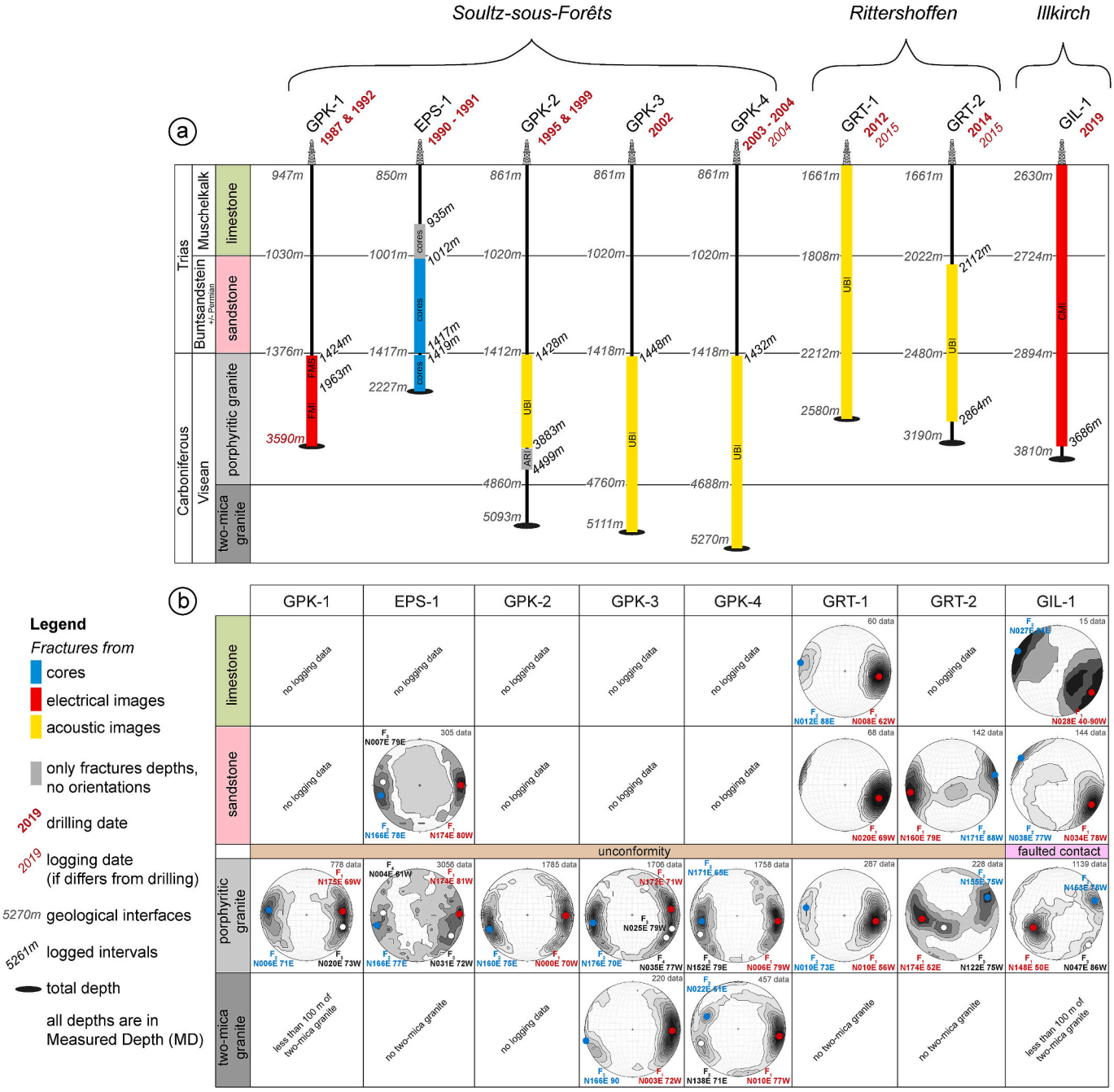

Fig. 2. a) Type of data available in each geothermal well, specifying the depth of the logged interval, the depth of the main geological interfaces, the drilling date and the logging date. b) Stereoplots (Schmidt lower hemisphere) per lithology in each geothermal well. The main fracture set is in red, the secondary set is in blue and the less represented one is in black. (For interpretation of the references to colour in this figure legend, the reader is referred to the Web version of this article.)

Alpine push reactivates ENE-WSW and NNE-SSW structures (Villemin and Bergerat, 1987; Ziegler, 1992; Schumacher, 2002; Dèzes et al., 2004) (Fig. 1b). Then, from the late Eocene to the early Oligocene, an E-W extension with N–S and NNE-SSW faults dominates the rifting phase (Doebl, 1967). At the late Oligocene, a NE-SW compression reactivates the border faults with dextral shear (Villemin and Bergerat, 1987; Schumacher, 2002). At the early Miocene, a NE-SW compression influenced by the Pyrenean push transforms the graben in a shear zone (Illies

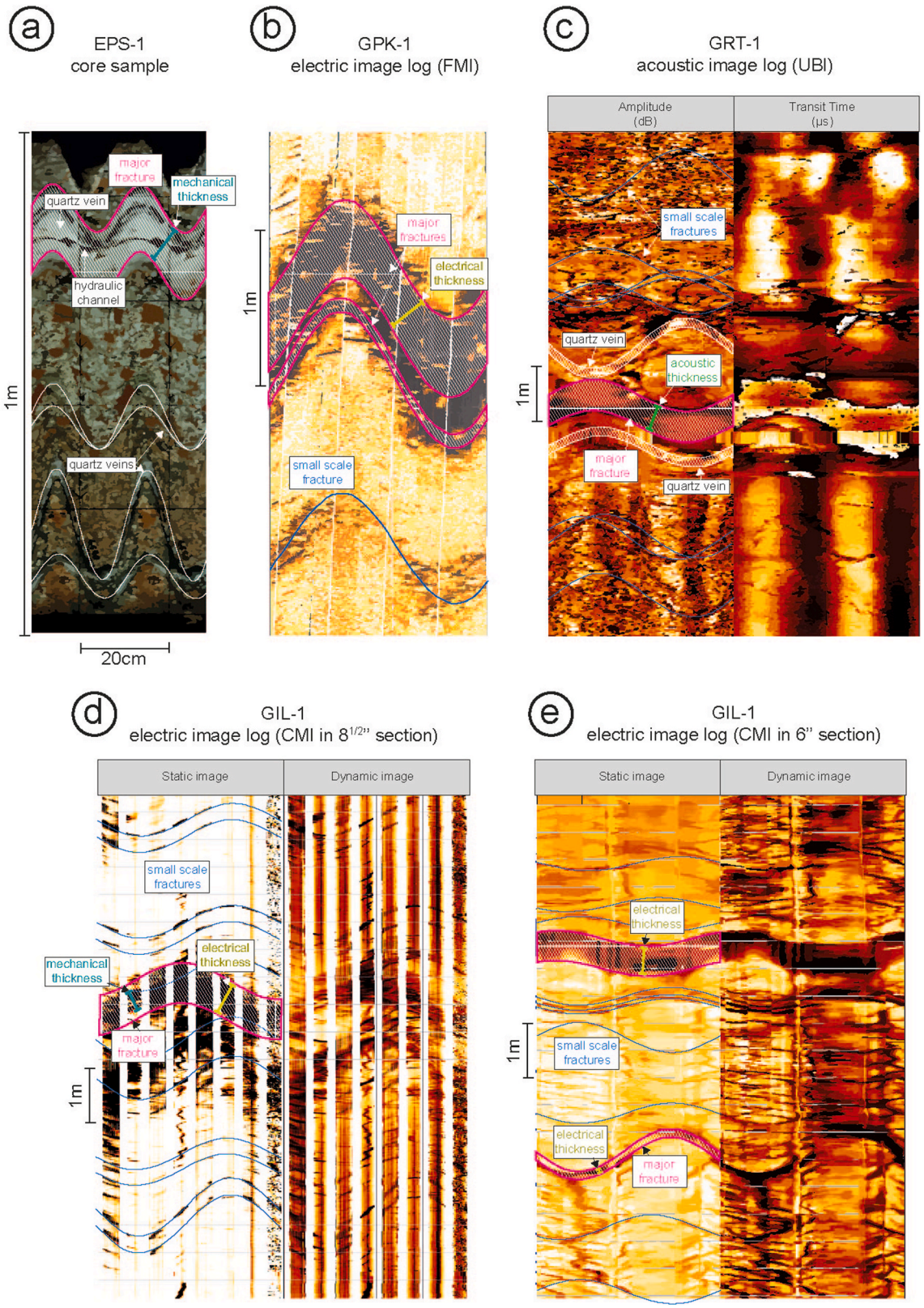

Fig. 3. Examples of borehole imagery methods and continuous cores: a) Core section of the EPS-1 well at 2156 m MD; b) FMI in the GPK-1 well at 2865 m MD; c) UBI in the GRT-1 well at 2321 m MD; d) CMI in the GIL-1 well in the 8″1/2 section at 3226 m MD; and e) CMI in the GIL-1 well in the 6″ section at 3330 m MD.

and Greiner, 1979; Bergerat, 1985; Edel et al., 2006). The most recent tectonic event corresponds to the Alpine NW-SE compression, which uplifts and erodes the crystalline horsts (Vosges and Black Forest) and reactivates the N–S and NE-SW faults inherited from the Variscan and Tertiary eras, respectively (Illies, 1972; Dèzes et al., 2004; Edel et al., 2007). The actual phase reactivates the border faults of the URG in sinistral shear and has an opening effect on the NNW-SSE structures (Michon et al., 2003).

3. Materials and methods

3.1. Geothermal reservoir

3.1.1. Soultz-sous-Forêts geothermal project

Several deep wells were drilled into the Soultz-sous-Forêts horst structure, which is made of 1.5 km thick tertiary and secondary sediments and a deep crystalline naturally fractured basement (Fig. 2). The Soultz-sous-Forêts horst is bounded on its western region by a normal fault that shows a vertical offset of at least 500 m and is oriented N20°E (Kappelmeyer, 1991; Genter and Traineau, 1996). In the URG, the sandstones comprise Buntsandstein and Permian. Buntsandstein is deposited in a fluvial environment, is isopach and is approximately 350 m thick in the Soultz-sous-Forêts wells (Aichholzer et al., 2019). The Permian layer, which is a result of continental deposits, is the oldest sedimentary unit in the graben and overlies the granitic basement by filling the paleo-basins; thus, its presence and thickness are difficult to predict (Aichholzer, 2019). In the Soultz-sous-Forêts wells, it is approximately 35 m thick. The granitic basement at Soultz-sous-Forêts comprises a monzogranite with K-feldspar mega crystals containing locally high amounts of biotite, dating from 334.0 + 3.8/3.5 Ma and a two-mica granite, which also contains muscovite and dates from 327 ± 7 Ma (Stussi et al., 2002; Cocherie et al., 2004). Both Visean ages confirm that the granites were emplaced before the Sudete phase and, thus, keep the structural heritage of the latter. Even if the Permo-Triassic sandstones revealed some permeable fractured zones, the initial target of the Soultz-sous-Forêts project was to develop an artificial exchanger in the deepest granite, which is located 3.5 km under the top of the basement. Thus, several wells were drilled to 5 km deep and, surprisingly, intersected a permeable natural fracture network that channelized brine (Fig. 3a and b). A large-scale permeable fault has been identified in the granite with an orientation of N144°E and a dip of 65–70°W (Sausse et al., 2010). The deep well exploration has shown that the highest natural permeability was found in the shallowest reservoirs of the granite, which means between the top basement and 2 km. The lessons learned from Soultz-sous-Forêts lead to an evolution of the concept for the Rittershoffen project, where geothermal wells were drilled a maximum of 1 km below the top basement. To date, the Soultz-sous-Forêts site comprises 5 deep wells (Fig. 2), with three wells (GPK-2, 3 and 4) that contribute to produce 1.7 MWe for the electrical grid (Mouchot et al., 2019).

3.1.2. Rittershoffen geothermal project

The Rittershoffen wells, before reaching the granite, intersect approximately 400 m of Buntsandstein and 10 m of Ante-Annweiler Permian sandstone layers. In the granitic basement, the wells intersect only monzogranite, which is remarkably similar to the one encountered in the Soultz-sous-Forêts wells (Fig. 4). The Rittershoffen site comprises two wells, i.e., GRT-1, the injection well, and GRT-2, the production well, which produces 24 MWth for industrial use (Mouchot et al., 2019). The Rittershoffen project took advantage of the Soultz-sous-Forêts experience, and the target was the Rittershoffen normal fault, which is located approximately 15 km east of the western Rhenish border fault and is oriented N5°E based on subsurface geological data (Baujard et al., 2017). After the drilling of GRT-1 and the realization of a new 2D

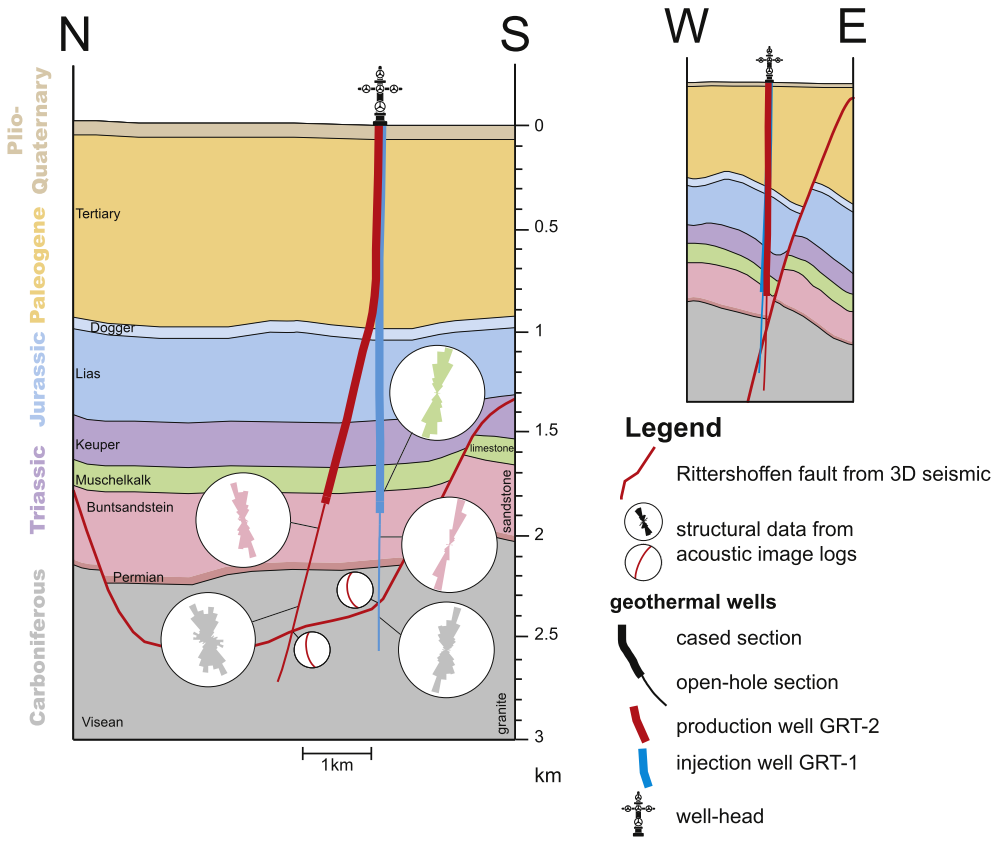

Fig. 4. Schematic geological cross-section drawn following the 3D seismic data, through the Rittershoffen geothermal site with the projection of the trajectories of the GRT-1 and GRT-2 wells. Only the local normal Rittershoffen fault is represented.

seismic campaign, the trajectory of GRT-2 was optimized according to the orientation of the Rittershoffen fault (Baujard et al., 2017). The second well is therefore slightly deviated but tangent to the local fault over its approximately 400 m length in the granitic basement (Fig. 4). Its high productivity index of 4 L/s/bar without any stimulation revealed a good connexion between the well and the fracture network (Baujard et al., 2017). The well probably intersects the fault zone characterized by a high fracture density with optimized natural fluid pathways (Vidal et al., 2017). The hydrothermal concept has been extremely positive for the GRT-2 well (Vidal and Genter, 2018).

3.1.3. Illkirch geothermal project

The Illkirch well, before reaching the basement, intersects 170 m MD (156 m TVD) of Buntsandstein, which is approximately 300 m thick in total (Aichholzer, 2019) (Fig. 5). No Permian is intersected due to the GIL-1 well trajectory, but the presence of Permian was found to be between 50 and 200 m in the deep wells in the near wells (Housse, 1984; Richard et al., 2016; Aichholzer, 2019). The granitic basement intersected by the GIL-1 well comprises monzogranite, which seems to be similar to the one encountered in the Soultz-sous-Forêts and Rittershoffen wells and is sometimes enriched with biotite. The target of the Illkirch project was the Eschau normal fault oriented N10°E based on 2D seismic interpretation (Richard et al., 2016), which is intersected by the well at the interface between Triassic sandstone and granite (Fig. 5). In the open-hole section of the well, the GIL-1 well was drilled in the NW-SE azimuth to intersect the fault at a high angle. To date, hydraulic tests tend to show that the permeability is mostly located in the deepest fractured granite.

These three geothermal sites explored by deep drilling have penetrated from 1 to 3.5 km into a deep fractured basement. To date, the Soultz-sous-Forêts and Rittershoffen sites are exploited for energy production, whereas at the Illkirch site, only one well has been drilled. Various techniques have been used for collecting high quality fracture datasets, such as continuous coring and electric/acoustic borehole images. These datasets have been collected in all the wells, thus providing the opportunity to compare the structural characteristics, such as the fracture orientation, fracture density, fracture spacing, fracture thickness and fracture permeability.

3.2. Structural analyses

3.2.1. Core samples

At Soultz-sous-Forêts, in the EPS-1 well, the structural data of 810 m of continuous coring from 1420 to 2230 m was analysed by (Genter and Traineau, 1996) (Fig. 3a). Approximately 3000 macroscopic natural fractures were identified, and 97% of them where successfully reoriented by comparing the core and acoustic borehole imagery. The orientations, depths and thicknesses of the natural fractures, as well as the type of secondary fillings (quartz, haematite, carbonates, clay minerals, chlorite, epidote, barite, anhydrite, pyrite and galena) were described with great care (Genter and Traineau, 1996).

3.2.2. Acoustic image logs

The Ultrasonic Borehole Imager (UBI) developed by Schlumberger in 1990 comprises a rotative transducer emitting an acoustic wave towards the borehole wall that records the amplitude and transit time of the wave after its reflection from the rock (Zemaneck et al., 1970). Acoustic imagers allow an image to be obtained that covers 100% of the borehole circumference (Fig. 3c). The UBI images are presented with an image in amplitude (dB), which provides information on the borehole roughness and quality, and an image in transit time (μs), which measures the distance between the tool and the borehole and informs on the borehole geometry (Serra and Serra, 2000). The colour scale shows the borehole expansions due to fractures and caves in dark colours (black), and the unaffected standard borehole diameter appears in light colours (yellow-orange). Natural fractures appear as sinusoids on the unrolled UBI images, which allows the dip, orientation and thickness of the fractures to be measured (Fig. 3c). The UBI log is oriented and the natural fractures measured on the images are then corrected with the borehole trajectory.

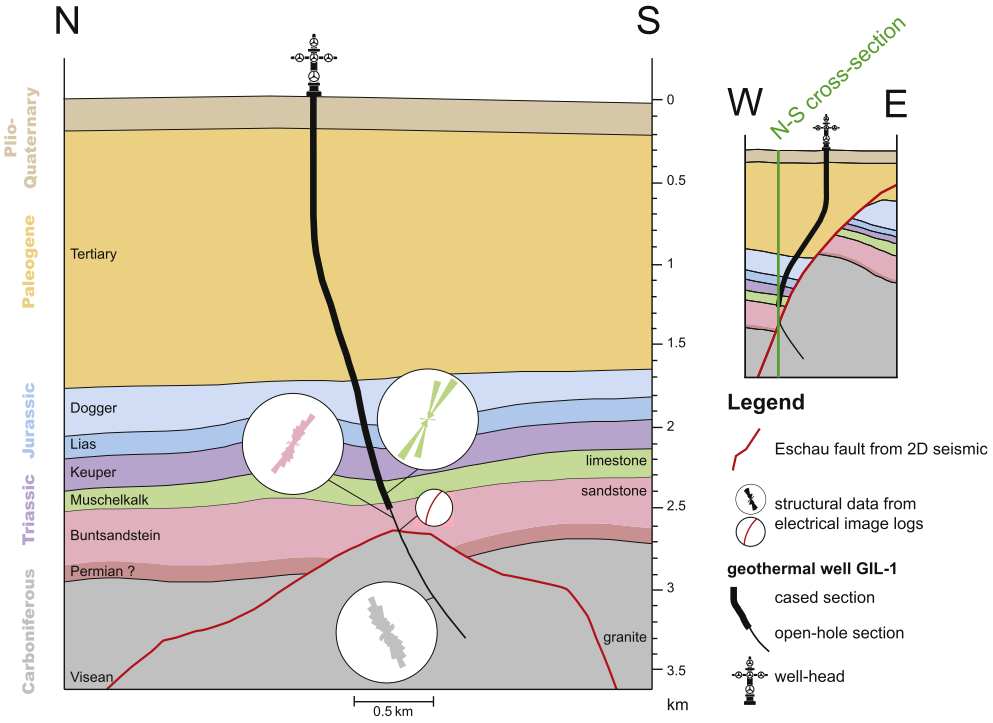

Fig. 5. Schematic geologic cross-section drawn following the 2D seismic data, through the Illkirch geothermal site with the trajectory of the GIL-1 well. Only the local normal Eschau fault is represented. The occurrence of the Permian sedimentary layer is uncertain because it was not intersected by GIL-1 but was observed in the surrounding wells (Aichholzer, 2019).

3.2.3. Electrical image logs

Resistivity image logs were developed by Schlumberger in 1986 as the Formation Micro-Scanner (FMS), which evolved into the Formation Micro-Imager (FMI) (Fig. 3b). To date, other companies, such as Weatherford, have developed similar tools, such as the Compact Micro-Imager (CMI). These various tools all comprise dipmeter pads, which comprise electrodes, which allow each pad to record the number of microresistivity curves that corresponds to the number of electrodes (Schlumberger, 1993; Crain, 1998). The number of pads increased during the evolution of the tool to reach 8 pads today, covering 80% of the borehole circumference in an 8" hole size (Fig. 3c, Table 1). The resistivity images are presented with a static and a dynamic image, where the static image is normalized over the complete depth interval logged; thus, the contrast responds to large-scale variations in lithology, porosity and saturation, whereas the dynamic image is normalized using a sliding window of 0.5 m; this highlights small-scale variations in the electrical contrast due to bedding, fractures, and changes in porosity (Fig. 3d and e). As on the UBI images, natural fractures appearing as sinusoids are measured and reoriented in the same way. The colour scale shows resistive materials in light colours (yellow-orange), whereas conductive materials appear in dark colours (black). As both the very saline brine and the clay minerals are very conductive, a black fracture on both the static and dynamic images could even be interpreted as an open fracture with very saline and conductive brine, or as a clogged fracture filled by conductive secondary clay minerals.

The Azimuthal Resistivity Imager (ARI) was developed by Schlumberger in the early 90's. It is a dual laterolog array with 12 azimuthal electrodes incorporated in its upper electrode, which provide a dozen deep oriented resistivity measurements in addition to the standard deep and shallow readings (LLD and LLS) (Schlumberger, 1993) (Table 1). The data is then displayed as an azimuthal resistivity image (Schlumberger, 1993) (Fig. 3). This image has much lower spatial resolution than the other acoustic or electrical images, but the interest is to use it as a complement to the other types of imageries, as its sensitivity to features beyond the borehole wall is higher. In the GPK-2 well, the ARI was acquired separately, and thus, only the depth of the fractures could be described.

3.2.4. Spatial resolution of fracture analysis

The different tools used for this study have roughly the same resolution, except for the core samples and the ARI (Table 1). It has been shown that even equivalent resolution borehole imagery techniques are not as exhaustive as the core data and cannot provide a complete characterization of the fracture network, as discrete fractures thinner than 1 mm are not properly detected and fractures closer to 5 mm appear only as single traces (Genter et al., 1997). However, for all techniques, the fracture orientation was shown to be correctly sampled (Genter et al., 1997). More precisely, Crain (1998) found that when comparing the same generation tools, the electrical images are more accurate than the acoustic images, even if the electrical images only cover 80% of the borehole circumference. The ARI is also the imagery method with the lower resolution, but it allows the detection of features and perturbations beyond the borehole wall; there is interest in using this in parallel with other electric or acoustic images. Usually, fractures from the Soultz-sous-Forêts and Rittershoffen datasets are classified according to their visibility on the image logs, for example, if they are visible on 100%, 50%, or 30% of the image, or if they are uncertain (Dezayes et al., 2010; Vidal et al., 2016, 2019). For this study, all the fractures classified as "uncertain" or visible on less than 50% of the image logs were not considered.

3.2.5. Fracture thickness

During the drilling, a mechanical erosion of the surface of the fracture rims would usually occur. Regardless of the imagery technique, this effect overestimates the natural fracture thickness because the fractures appear larger on the image than in reality. This effect does not exist on

Table 1
Description of the specificities of each method used for the structural data analysis. The well logged, the logging date, the tool configuration, the vertical and azimuthal resolutions, as well as the references are detailed for each method used.

Tool name	Core	UBI	ARI	UBI	UBI	FMS	FMI	CMI
Well logged Logging date	EPS-1 1990–1991	GPK-2 1995	GPK-2 1999	GPK-3 GPK-4 2002 2004	GRT-1 GRT-2 2015	GPK-1 1987	GPK-1 1992	GIL-1 2019
Tool configuration	Core mining Diameter: 78 mm from 930 to 1995 m and 56 mm from 1995 to 2230 m	Transducer inserted in a rotating sub	12 azimuthal electrodes	Transducer inserted in a rotating sub	Transducer inserted in a rotating sub	2 pads with 29 sensors/pad and 2 pads with 2 sensors/pad = 62 sensors	8 pads with 16 sensors/pad = 64 sensors	8 pads with 22 sensors/pad = 172 sensors
Vertical resolution	<1 mm	10 mm	200 mm	10 mm	10 mm	3 mm	2.5 mm	5 mm
Azimuthal resolution	<1°	1.6°	30°	2°	2°	2.2°	1.5°	±5°
References	Genter and Traineau (1996)	Genter et al. (1997)	(Sausse and Genter, 2005; Schlumberger, 1993) rajouter rapport (Henriksen, 2001)	Valley (2007)	Vidal et al. (2017)	(Genter et al., 1997; Sausse and Genter, 2005)	(Genter et al., 1997; Sausse and Genter, 2005)	Schlumberger (1993)

core samples, especially with a core recovery close to 100%, as we had in EPS-1 (Fig. 3) (Genter and Traineau, 1996). Then, the different imagery and coring techniques do not precisely consider the same fracture thicknesses scale.

- For the core samples, we measure the mechanical thickness, which corresponds to the normal distance between the two consecutive walls of a given fracture (Fig. 3a). All the natural fractures observed at Soultz-sous-Forêts are mineralized with secondary minerals, such as quartz, clay minerals, barite, and calcite. Thus, the fracture thickness corresponds to the clogged thickness and could include the residual fracture hydraulic aperture if the clogging is incomplete (Fig. 3a). On EPS-1 cores, less than 1% of the natural fractures present incomplete clogging by hydrothermal minerals. From the EPS-1 core analyses, 3000 fractures are characterized, and all the natural fractures are systematically filled by at least one or several secondary hydrothermal minerals (Genter and Traineau, 1996).
- Regarding the electrical images, the electrical thickness includes the clogged fracture and its nearby hydrothermally altered environment, corresponding to the beginning of the damage zone (Fig. 3b, d & e). It matches our geothermal wells in basement rocks to clay minerals, such as illites, that have the same electrical signature as the fracture itself, generally filled by illite or a conductive fluid. Thus, it becomes quite difficult to differentiate the precise trace of the fracture on the borehole wall. If we add potential mechanical erosion due to the drilling processes, we assume that the fracture thicknesses observed on the electrical images are potentially larger than those on the core samples. The hydraulic aperture, if it exists, is included in this electrical thickness. The electrical thickness tends to be larger than the mechanical thickness.
- Regarding the acoustic images, the acoustic thickness includes the clogged fracture closer to the mechanical thickness but does not systematically include its nearby altered environment (Fig. 3c). The hydraulic thickness, if it exists, is included in this acoustic thickness. According to the cases, the acoustic aperture can be larger or smaller than the mechanical aperture (Genter et al., 1992; Vidal et al., 2017).

4. Results

4.1. Fracture orientation

4.1.1. Soultz-sous-Forêts

The orientation of the natural fracture set is quite similar in the Soultz-sous-Forêts wells to a conjugate fracture set striking N000 E ± 10° and highly dipping (Fig. 2b) (Dezayes et al., 2010). In all the Soultz-sous-Forêts wells and in all the formations, the main fracture set dips to the West. In the Buntsandstein, the fracture data available are exclusively from the core samples of the EPS-1 well and express a conjugate set comprising fractures striking N170°E and steep dips of 80° (Fig. 3). In the monzogranite, the fracture data are from the 5 wells and behave in the same way as the conjugate set in the Buntsandstein but with less steep dips of 75° (Fig. 3). In the deeper two-mica granite, the fracture set striking N000 E ± 10° and dipping to the West is more visible (Fig. 3).

4.1.2. Rittershoffen

In both the GRT-1 and GRT-2 wells, the fractures roughly strike in the N–S direction but a divergence of dip is observed between both wells (Figs. 2b and 4). In the GRT-1 well, the main set dips to the West, whereas in the GRT-2 well, the main set dips to the East (Figs. 2b and 4). In the Muschelkalk, fracture data are only available in the GRT-1 well and show a main fracture set oriented N006°E and dipping 62°W (Fig. 3b). In the Buntsandstein, fracture data for both wells are available, in the GRT-1 well a fracture set strikes N020°E and dips 69°W, which is quite different from the conjugate fracture set observed in the GRT-2 well, which strikes N160-170°E and steeply dips 88°W and 79°E (Fig. 3b). In the granite, the GRT-1 well presents a conjugate fracture set that strikes N010°E and dips 56°W and 73°E; the GRT-2 well also presents a conjugate fracture set, but it is oriented N155-174°E and has dips 75°W and 52°E, which are associated with a minor fracture set striking 122°E and dipping 75°W (Fig. 3b).

4.1.3. Illkirch

At Illkirch, the fracture data results from the GIL-1 well, where the fracture orientation in the sediments strikes NE-SW, but differs from those observed in the granite that strikes NW-SE (Figs. 2b and 5). In the sediments, the main fracture set dips to the West whereas in the granite, it dips to the East (Figs. 2b and 5). The fractures in the Muschelkalk are highly dispersed due to the small amount of data collected and present a nearly-vertical conjugate set striking N028°E (Figs. 2b and 5). In the Buntsandstein, the fractures also present a conjugate set but strike approximately N035°E with a steep dip of 80° (Fig. 2b). In the granite, a conjugate set striking N148-163°E and dipping 76°W and 48°W is observed (Fig. 2b). Note that the Eschau fault was intersected by the well with a local orientation of N30°E and a general orientation of N10°E from the 2D seismic data.

4.2. Permeable fractures

All the geothermal wells presented in this paper intersected natural fractures considered as permeable. A natural fracture was considered permeable if there was at least a temperature anomaly and another permeability indicator, such as mud losses or outlets, and gaz anomalies (Evans et al., 2005; Vidal et al., 2017, 2018, 2019). In this study, we only included natural fractures that were already permeable prior to any type of stimulation. The permeable fractures with their structural data and the associated permeability indicators are presented in the supplementary materials. However, it is important to consider that these permeable fractures are most often within a larger fracture zone (FZ). They generally act as the main fluid pathways of the FZ, are easily detected on core samples or in image logs and are surrounded by a damage zone (Fig. 3) (Genter et al., 2000; Vidal et al., 2017; Vidal and Genter, 2018). The permeable FZs in the granite from Soultz-sous-Forêts and Rittershoffen were deeply developed by Vidal et al. (2019) and Dezayes et al. (2010) and those in the sediments were developed by (Vidal et al., 2015, 2017).

At Soultz-sous-Forêts, in the GPK-1 well, 4 permeable FZs were detected in the granite, 1 in the Buntsandstein, 2 permeable but partly sealed FZs were also observed in the Muschelkalk and the Keuper. In the EPS-1 well, 1 permeable FZ was detected in the granite and 1 in the Buntsandstein. In the GPK-2 well, 6 permeable FZs were detected in the granite, 1 in the Buntsandstein and 2 in the Muschelkalk. In the GPK-3 well, 5 permeable FZs were observed in the granite, 2 in the Buntsandstein and 2 in the Muschelkalk. In the GPK-4 well, 7 permeable FZs were detected in the granite, 1 in the Buntsandstein and 1 in the Muschelkalk.

At Rittershoffen, in the GRT-1 well, 2 permeable FZs were detected in the granite and 1 in the Muschelkalk. In the GRT-2 well, 4 permeable FZs were observed in the granite, 1 in the Buntsandstein and 1 in the Permian.

At Illkirch, in the GIL-1 well, permeable FZs were detected in the electrical image logs. In the granite, 6 permeable FZs were detected from 3050 to 3090, 3210 to 3230, 3309 to 3315, 3330 to 3390, 3500 to 3575, and 3625–3645 m MD. They are all associated with a temperature anomaly (Glaas et al., 2021). Surprisingly, the fracture considered as the intersection of the Eschau fault does not present a temperature anomaly and, thus, is not considered as naturally permeable. On the other hand, a temperature anomaly is associated with the intrusion of the biotite-rich granite structures inside the batholith and suggest that dyke or sill could represent a heterogeneity and a localized permeability. Only one permeable FZ was intersected within the Buntsandstein in GIL-1 from 2780 to 2785 m MD.

More generally, in the 3 geothermal sites, we lack oriented data in the sedimentary part. Due to this lack, only 9 permeable fractures could be represented in Fig. 6b.

Permeable fractures are globally striking NNW-SSE (Fig. 6a). In the sediments, the permeable fractures present a conjugate set striking N175°E and dipping 75°E and W (Fig. 6b). In the granitic basement of Soultz-sous-Forêts, the permeable fractures intersected by the wells present a conjugate set striking N164°E and dipping 85°E and W (Fig. 6c). In the granitic basement of Rittershoffen, the permeable fractures intersected by the wells present a conjugate set striking N003-168°E and dipping 82°E and W (Fig. 6c). In the granitic basement of Illkirch, the permeable fractures intersected by the well present a conjugate set striking N149°E and dipping 86°E and W (Fig. 6c). For the three sites, the maximum horizontal stress direction is sub-parallel to the permeable fracture strike±10° (Valley and Evans, 2007; Hehn et al., 2016).

4.3. Fracture density

In the granite, the EPS-1 fracture set from the core samples presents the highest fracture density of 3.85 (Fig. 7b). The EPS-1 well presents two main sections; the first 150 m are highly fractured (6.7 frac/m), and the deepest section is less fractured (4.7 frac/m) (Fig. 7a).

The other wells present fracture datasets from the acoustic and electric image logs collected from the 3 geothermal sites. In the sandstone of the Buntsandstein, the fracture densities are low, from 0.40 to 0.66 frac/m, whereas in the granite, they show a wide range of fracture density values from 0.36 to 1.60 frac/m. In the granitic basement, the cumulative fracture densities were separated in several depth interval sections, which are roughly the same for all the wells (Fig. 7a and b). More precisely, GIL-1 and GPK-2 show quite similar fracture density values, i.e., 1.6 frac/m for GIL-1 and 1.2 frac/m for GPK-2 in the first 900 m of the granitic basement. GIL-1 does not descend deeper into the granitic basement, but below, in GPK-2, two different sections are observed, as follows: from 900 to 1800 m and from 1800 to 3000 m below the top of the granitic basement, where the fracture densities are of 0.6 and 0.2 frac/m, respectively. GPK-3 and GPK-4 show exactly the same depth interval sections with similar ranges of fracture densities (Fig. 7). Both wells can be separated into 4 distinct depth sections, as follows: the first 450 m show fracture densities of 0.8 and 0.9 frac/m, respectively; from 450 to 1350 m below the top basement, the fracture density is of 0.4 frac/m; from 1350 to 1920 below the top basement, the fracture density is of 0.8 frac/m for both wells; and from 1920 to 3000 m below the top basement, the fracture density values are of 0.4 and 0.2 frac/m, respectively. This last depth interval is also observed in the GPK-2 well, which also has a fracture density of 0.2 frac/m. However, the deepest part of GPK-2, representing a length of approximately 600 m, was never characterized with borehole image logs due to the borehole conditions. GPK-1, which is characterized by fracture data interpreted from former electrical image logs (FMS & FMI), presents the lowest fracture density value of 0.36 frac/m in the granite (Fig. 7b).

From a general point of view, we observe that the fracture density versus depth is higher in the first 500–1000 m of the granitic basement and that from 1900 to 3000 m below the top basement of Soultz-sous-Forêts, the fracture density is lower. GRT-1 presents a fracture density very similar to GPK-2, 3 and −4 in the granitic section (0.57), whereas it is slightly higher for GRT-2 (0.79) (Fig. 2b).

4.4. Fracture spacing

To facilitate a comparison, the fracture spacing curves in the granite were normalized for all the wells by applying a correction factor that was determined by dividing each well section by the longest available well section in the basement. The longest well section where fracture data are available is the GPK-4 well granitic section, which is 3831 m. For each well, this correction factor was applied to the fracture spacing distribution plotted on a log-log scale (Fig. 8). The maximal spacing can be estimated by the projection of the distribution curve on the horizontal axis. We observe that all the largest fracture spacings converge towards a pluridecametric value ranging between 20 and 80 m, except for EPS-1, GPK-2 and GRT-1, where the largest spacing tends to converge to values higher than 100 m (Fig. 8). The coefficients of variation (CV) were also calculated for each well by dividing the standard deviation by the average (Fig. 8). All the wells present CV values higher than 1, which is usually associated with a clustered organization of spacing, meaning a heterogeneous distribution of the fractures along the depth, with closely spaced fractures alternating with large spaces between the fractures. The higher the CV, the more the organization is clustered (Odling et al., 1999; Gillespie et al., 2001).

The fracture spacing distribution for EPS-1 fits a perfect straight line on the log-log graph for more than two decades (Fig. 8a), which means that the fracture spacings are governed by a power law having an exponent of −1.07. As the resolution of the fracture analysis with core samples is the highest, it means that the sampling biases are minimized. Thus, the power law distribution and the highest CV for fracture spacings, which is 5.56 in the basement, reflects a highly heterogeneous fracture distribution in the rock mass (Fig. 8).

With the example of the Rittershoffen wells where the same UBI was used, we can also compare the results obtained in terms of the fracture spacing distribution (Fig. 8c and d). GRT-2 presents a negative exponential law with the lowest CV (1.21), which reflects a low clustered organization of fractures in the well (Fig. 8d), whereas GRT-1 presents a power law, which reflects a fracture distribution in clusters (Fig. 8c). Geologically, it is assumed that GRT-2 tangentially intersects the local

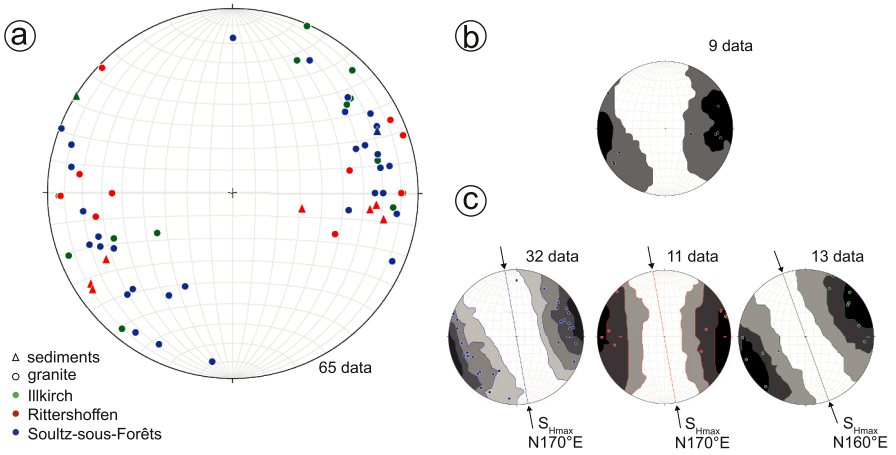

Fig. 6. Stereoplots (Schmidt lower hemisphere) of the permeable fractures in the sediments (regrouping Buntsandstein sandstones and Muschelkalk limestone) and in the granite; the orientations and dips used in this figure are detailed in the supplementary materials S1. a) Poles of all the permeable fractures. b) Stereoplot of the permeable fractures in the Muschelkalk and Buntsandstein. c) Stereoplot of the permeable fractures in the granite at Soultz-sous-Forêts, Rittershoffen and Illkirch (from left to right); SHmax is the maximum horizontal stress orientation (Valley, 2007; Hehn et al., 2016).

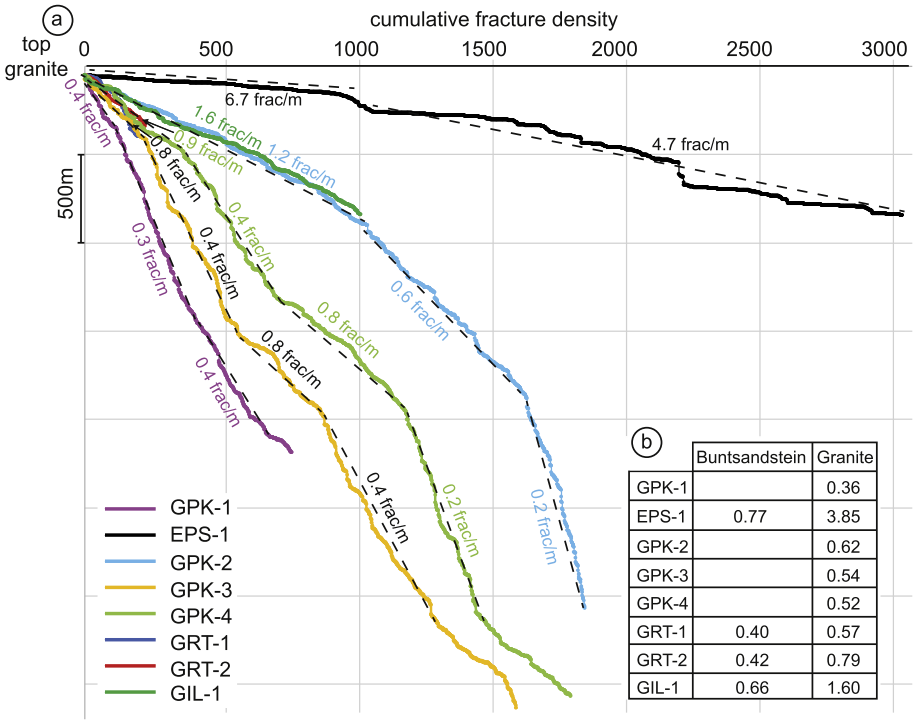

	Buntsandstein	Granite
GPK-1		0.36
EPS-1	0.77	3.85
GPK-2		0.62
GPK-3		0.54
GPK-4		0.52
GRT-1	0.40	0.57
GRT-2	0.42	0.79
GIL-1	0.66	1.60

Fig. 7. a) Cumulative fracture density along the depth for all the geothermal wells. The cumulative fracture density is presented only in the granite, and the depth scale was normalized to begin at the top of the granite for all the wells. b) Table presenting the global fracture densities (frac/m) in the Buntsandstein sandstones and the granite for each well.

Rittershoffen normal fault at a 400 m thick section through its damage zone. This assumption means that an intermediate density of fractures of 0.79 frac/mm (Fig. 7b) over several hundreds of metres in accordance with the distribution law is encountered. In contrast, GRT-1 crosses the fault perpendicularly to enter the low altered granite associated with a lower fracture density (0,57 frac/mm, Fig. 7b), which could validate the heterogeneous fracture distribution and cluster organization, as observed in Fig. 8c and d. Note that a truncation bias is visible at the end of the curve of GRT-1 because the length of the studied section is not long enough for a complete sampling (Fig. 8c). The other bias is the censoring, which is visible at the beginning of the curve and is explained because fractures that are too closely spaced cannot be sampled with the borehole imagery technique, unlike with the core sample (Odling et al., 1999; Gillespie et al., 2001). In fact, censoring is visible on all the curves excepted on the EPS-1 curve, where all the closely spaced fractures are correctly detected and sampled (Fig. 8a). Due to the effects of truncation and censoring, the power law of GRT-1 fits approximately one decade (Fig. 8c). Surprisingly, GRT-1 fits a power law but has a low CV (1.84), which could be explained by the fact that the effects of censoring and truncation are important. These observations show that the fracture distribution is well represented by the law but that the tool resolution can influence the CV value.

In GIL-1, the fracture distribution fits a negative exponential law quite well, which means that the fracture spacings are more homogeneously distributed, as in the GRT-2 well (Fig. 8b and d). Maybe the fit between the raw curve and the extrapolated law is not perfect because of the electrical tool resolution for GIL-1, which is higher than for the acoustic tool for the other wells, enabling the sampling of the closest fractures. It could more accurately reflect the "natural system" in GIL-1 than in GRT-2, for example. In the case of GIL-1, the low CV (1.74) is in agreement with its fit with a negative exponential law, reflecting a low clustered fracture distribution of spacings (Fig. 8b).

4.5. Fracture thickness

In Fig. 9, the fracture thickness is represented as cumulated along the depth for the three geothermal sites. The permeable fractures identified by various techniques in the corresponding wells were superimposed on the curves as coloured disks (Fig. 9).

In GPK-3, GRT-1 and GRT-2, the curves show stair-like trends, with the plateau parts showing zones with high cumulated fracture thicknesses and the vertical parts showing zones with lower cumulated fracture thicknesses (Fig. 9a and b). This indicates the existence of a fracture thickness distribution in clusters of intensively clogged fractures and zones depleted in fractures with very high clogging. For EPS-1, some steps are also observed (Fig. 9a) that correspond to high fracture thickness zones that were observed on cores (Sausse et al., 1998). For the GIL-1 well, the curve trend is slightly different, with a fracture thickness distribution that shows a rather regular slope with depth. It could correspond to a regular distribution with depth of thicker natural fractures (Fig. 9c).

At Soultz-sous-Forêts, in the EPS-1 well, the fracture thickness curve presents two plateaus, i.e., one at 1600 m TVD and one at 2150 m TVD, which are associated with permeable FZs (Fig. 9a). The thickest secondary quartz filling was observed in a permeable FZ with an apparent fracture thickness of 40 cm, located at 2174 m, and it is found in the deepest plateau (Figs. 3a and 9a) (Genter et Traineau, 1996). In the GPK-3 well, there are at least 10 plateaus, and we observe that the permeable FZs are systematically related to the thickest fractures (plateau) (Fig. 9a). In contrast, thicker fractures are not systematically naturally permeable, for example, at 3200 m TVD. In the GPK-3 well, from the top basement to 2100 m TVD, the fractures are thicker and 4 of the 5 permeable fractures are concentrated in these 600 first metres of the granitic basement (Fig. 9a). The most permeable FZ is located in GPK-2 at 2100 m TVD and shows hydraulic index of 20 L/s/bar (Jung et al., 2010; Schill et al., 2017). In GPK-3, below this FZ, there is a drop in the fracture thickness, except at 4770 m TVD, where there is a cluster of thick fractures associated with high natural permeability controlling

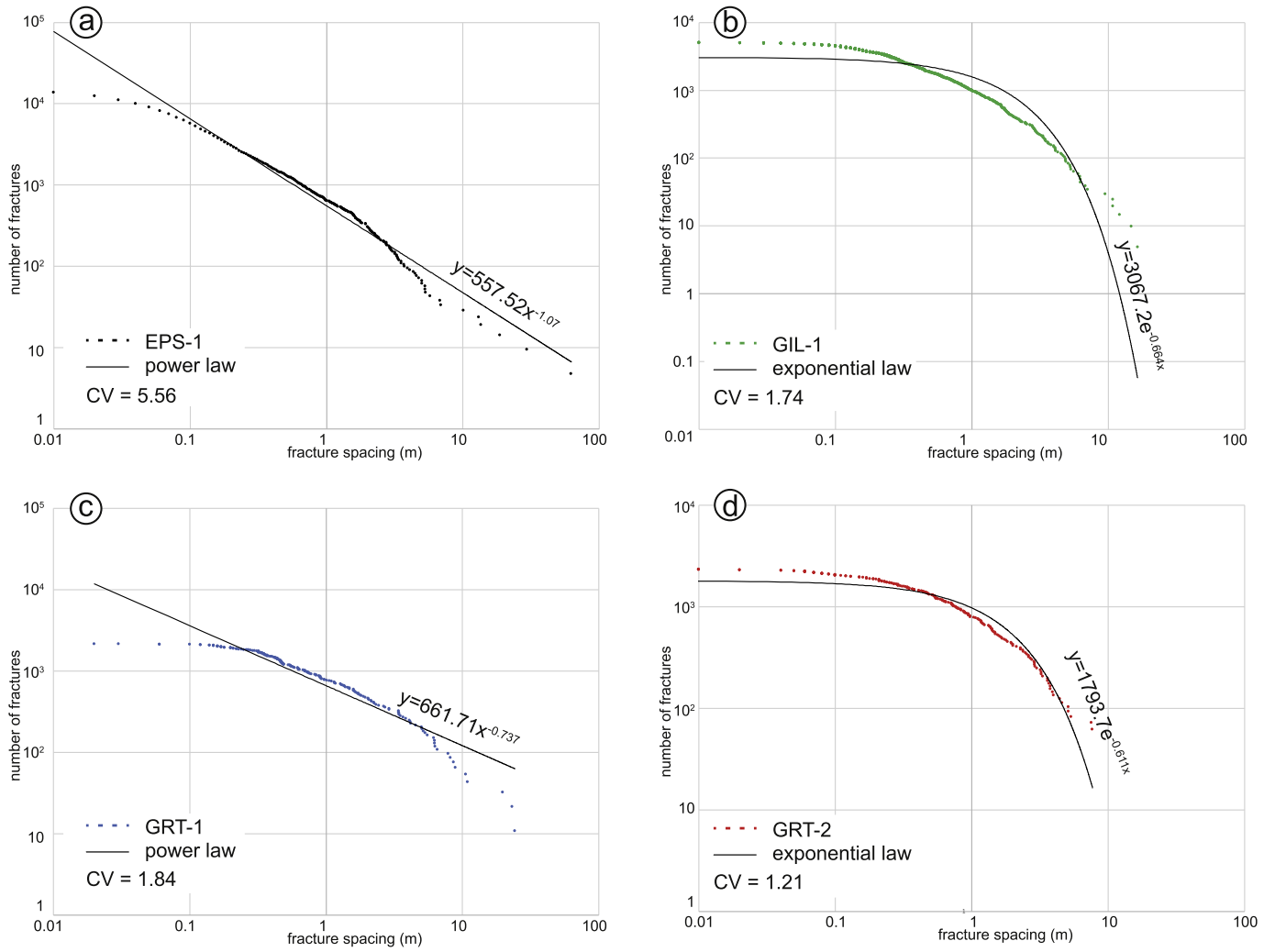

Fig. 8. Fracture spacings presented on a log-log scale, with the type of law fitting the data and its equation, and the coefficient of variation (CV): a) For the EPS-1 well; b) For the GIL-1 well; c) For the GRT-1 well and d) For the GRT-2 well.

70% of the natural flow (Gentier et al., 2005; Sausse et al., 2010).

At Rittershoffen, in the GRT-1 well, we observe a dozen plateaus, and slightly less are observed in the GRT-2 well (Fig. 9b). In the GRT-1 well, both the permeable FZs are associated with plateaus, and in the GRT-2 well, the permeable FZs are not systematically linked to plateaus. In the GRT-1 and GRT-2 wells, until 2300 m TVD, the fracture thickness is small, except at 2270 m TVD in GRT-1 and 2260 m TVD in GRT-2. From 2300 to 2400 m TVD, we observe a thick fracture filling, which means between 100 and 200 m below the top basement. The Rittershoffen fault is supposed to be intersected by the GRT-1 well at 2328–2368 m MD (2312–2352 m TVD) and by the GRT-2 well at 2766–2800 m MD (2382–2410 m TVD) (Vidal et al., 2017). In the granite in the GRT-2 well, 5 of the 7 permeable fractures are located in this interval. In the granite of the GRT-1 well, both permeable fractures are also located in this interval. Another interesting observation is that between 2200 and 2300 m, the cumulative fracture thickness is extremely low for these 2 wells. This interval corresponds to the propylitic monzogranite, which is very slightly altered. The fracture thickness is extremely low in this interval, except for the top basement, which is a reddish granite from 2170 to 2200 m TVD in GRT-2 and from 2215 to 2222 m MD TVD in GRT-1. The top of the reddish granite contains thicker fractures and is altered with a reddish colour, which is clearly because of paleo weathering (Glaas et al., 2018; Vidal and Genter, 2018).

At Illkirch, GIL-1 shows a quite regular fracture thickness distribution with depth, and there is no plateau trend, contrary to the Soultz-sous-Forêts or Rittershoffen wells (Fig. 9c). The permeable fractures are not related to the thickest fractures (Fig. 9c). However, we can observe a slightly higher fracture thickness from 2700 to 2830 m TVD, which means between 40 and 200 m below the top basement. Although a high fracture thickness is observed in the GIL-1 well, only 2 of the 13 permeable fractures are located in these first 200 m of the granitic section. The 11 other permeable fractures are located far below the first 200 m of the granitic basement. All permeable fractures are localized in sections where there is a high cumulative fracture thickness, except at 3185 and 3189 m TVD.

We calculated the fracture thickness densities expressed in mm/m for each well (Table 2). Surprisingly, the fracture thickness density is the lowest in EPS-1, with approximatively 5 mm/m. This could be due to the method of measuring the fracture thickness, which is very accurate on cores compared to the electrical or acoustical methods, which could overestimate the fracture thickness. GRT-2 presents the lowest fracture thickness density (8.8 mm/m), and the GRT-1 density is slightly higher (13.4 mm/m). The GPK-3 and GIL-1 wells show quite similar fracture thickness density values of approximately 2 mm/m in the first 800 m; this is the highest value and is 4 times higher than that of EPS-1 and is approximately 2 times higher than that of the GRT-1 well. In the GPK-3 and GIL-1 wells, we see that the fracture thickness density is higher in the top portions of the granite (20 and 29 mm/m respectively) than in its deepest sections (4.3 and 20 mm/m respectively). The mean values of the fracture thicknesses were also calculated (Table 2). In the first 800 m

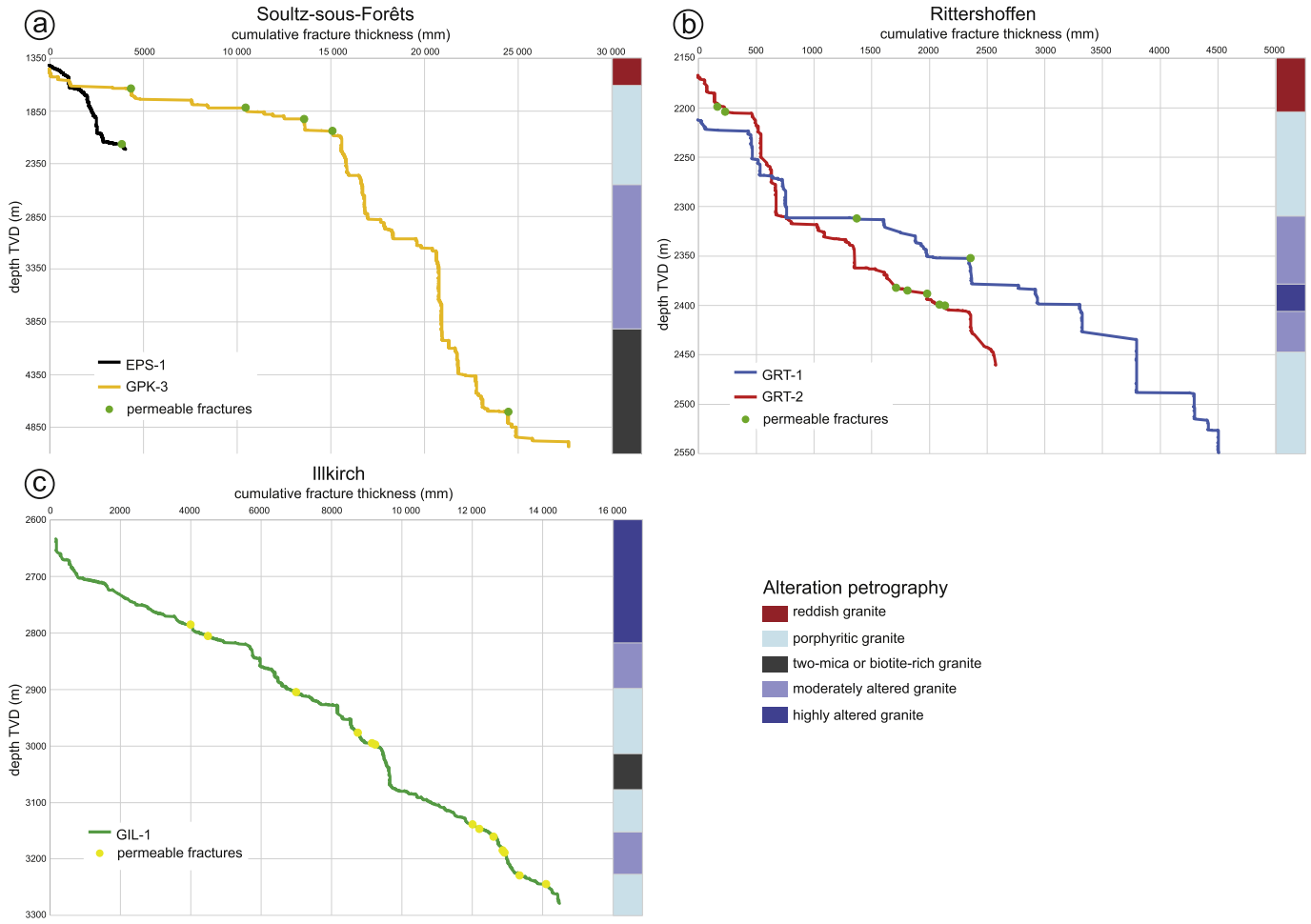

Fig. 9. Cumulative fracture thicknesses presented along the depth (TVD) for the 3 geothermal sites, with the main petrographical units along the depth showing the alteration grades or mineralogy of the granite,: a) For Soultz-sous-Forêts with the EPS-1 and GPK-3 wells; b) For Rittershoffen with the GRT-1 and GRT-2 wells; and c) For Illkirch with the GIL-1 well.

Table 2
Fracture thickness densities and mean values of the fracture thicknesses calculated for the EPS-1, GPK-3, GRT-1, GRT-2 and GIL-1 wells. For the GPK-3 well, the top of the granitic section corresponds to the first 800 m of granite intersected by the well, and for the GIL-1 well, it corresponds to the 200 m of granitic section intersected by the well.

		EPS-1	GPK-3	GRT-1	GRT-2	GIL-1
Fracture thickness density (mm/m)	Granitic section	5.1 mm/m	7.8 mm/m	13.4 mm/m	8.8 mm/m	22.5 mm/m
	Top of the granitic section		20 mm/m			29 mm/m
	Deepest granitic section		4.3 mm/m			20 mm/m
Mean fracture thickness (mm)	Granitic section	4 mm	14.4 mm	18.5 mm	11.3 mm	14 mm
	Top of the granitic section		33.6 mm			19.8 mm
	Deepest granitic section		8.3 mm			12.4 mm

of the granite, the EPS-1 well presents the lowest value (4 mm), the GIL-1 and GRT-2 wells present average values (between 11 and 14 mm) and the GRT-1 and GPK-3 wells present higher values (18.5 and 33.6 mm, respectively).

5. Discussion

5.1. Is the permeability linked to the structural and hydrothermal inheritance?

We observe a vertical clockwise rotation of the fracture orientation in the studied wells from NNW-SSE/N–S in the underlying granitic basement to N–S/NNE-SSW in the overburden sediments (Fig. 2b). The nearly vertical fracture network intersected in the granite could be inherited from the late-Variscan tectonic history of the URG, whereas the sediments could be affected by more recent regional stress fields, mainly from the Cenozoic era. The direction of the fractures in the granite could correspond to that of the Variscan era. They could belong to a larger network of Variscan normal faults reactivated under the Pyrenean compression that took place at the Eocene era (Villemin and Bergerat, 1987). In the granite, a change of the dominating dip direction (E or W) depending on the wells and the depths is observed (Dezayes et al., 2010). It is interesting to notice that the geometry of the permeable fractures in the granite is well constrained with the main striking values; NNW-SSE for Soultz-sous-Forêts, N–S for Rittershoffen and NNW-SSE for Illkirch. These directions could correspond to structures

with dips approximately 70° (Fig. 2b), which could be associated with Variscan normal faults. They could be reactivated into shear faults under the Pyrenean compression at the Eocene or into normal faults under the Rhine Graben extension at the Oligocene (Villemin and Bergerat, 1987). However, in the sediments, the fracture orientation is slightly different from that in the granite but is more consistent with the Cenozoic stress field (Fig. 2b). In the sediments and the granite, permeable fractures strike from NW-SE to NNW-SSE, which could suggest that their present-day permeability is directly linked to the trans-tensional horizontal stress field because they are critically stressed (Evans et al., 2005) (Figs. 1b and 6c). They could tend to open both by dilatancy and by shearing, which are favourable conditions for permeability. Structural inheritance is guided by the geological tectonic history, which reactivated the same structural directions (NW to NNW). The ENE direction is poorly represented by the drilling data or other outcrop studies, while it is suggested to be a permeable direction by other large scale geophysical studies (Dezayes and Lerouge, 2019; Bertrand et al., 2020). This direction is interpreted as structures delimiting large blocks (Bertrand et al., 2020).

The inherited fracture directions and the actual stress orientation and magnitude are not the only factors that could explain the fracture permeability. In fact, it was observed in all the geothermal wells that the fractures in the granite are more permeable than those in the Triassic sandstones. For example, in GRT-2, it was demonstrated that the main hydraulic contribution comes from a FZ in the granitic basement, even if FZs with the same orientation were also intersected in the sediments (Baujard et al., 2017; Vidal et al., 2017). This could be linked to the internal organization of the FZ. Indeed, at the borehole scale, the FZs in the granite present a core with cm-thick open fractures that channelize the geothermal resource. These fractures systematically correspond to the thickest fractures encountered in the wells (Fig. 9). In addition to this structural inheritance, a hydrothermal inheritance is also predisposing the fracture permeability. The hydrothermal inheritance is due to the successive hydrothermal events that occur in the fracture network and provoke primary mineral dissolution and secondary mineral precipitation cycles. The residual effect is complex FZs with hydrothermally altered and porous damage zones of several m-thick, where intense fluid-rock ratios occurred and led to mineral infillings that could block the permeability over time. In the sediments, the fault core generally comprises thinner fractures and lower fracture densities. Thus, the resulting connectivity of the fractures is less important and hinders reaching interesting hydraulic properties from sedimentary hard-rocks for geothermal exploitation (Vidal and Genter, 2018). According to our extensive core observations, we consider the fracture thickness to be a good proxy for the fracture hydrothermal filling rate. In the Soultz-sous-Forêts and Rittershoffen wells, the cumulative fracture thickness versus the depth shows the occurrence of the thickest fractures partly filled by hydrothermal minerals, which alternates with FZs depleted of thick fractures. The occurrence of permeable fractures is systematically associated with the thickest fractures with residual channels. In contrast, in the Illkirch well, the fracture thickness is regularly distributed along the depth and there is no clear relation between the permeable fractures and their thicknesses. Our observations could then show that the permeability in the granite is associated with the thickest fractures with channels where an intense fluid-rock ratio occurred, producing thick fracture infillings but where the permeability is maintained over time. The most permeable well of this study (GRT-2, Rittershoffen) presents an average fracture density (0.79 frac/m) and the lowest mean fracture thickness (11.3 mm). This shows that the relation between permeability and fracture thickness is valid for a given wells but is less robust for inter-site well comparison. Indeed, the lowest permeable well of this study (GIL-1, Illkirch) presents the highest fracture density (1.60 frac/m) and a fracture thickness (14 mm) higher than GRT-2. The residual permeability of the fracture depends on the competing geochemical equilibrium between the dissolution and precipitation processes, which allows to preserve, or not, natural fluid channels. The local normal fault at the interface between the sandstone and the granite encountered at Illkirch probably underwent a very intense fluid/rock ratio, which generated primary mineral dissolution and secondary clay precipitation and clogged the residual permeability. The reason of a higher fluid/rock ratio in the Illkirch reservoir could be due to the local thermal or geochemical disequilibrium between the brine and the faulted rocks, including the Buntsandstein sandstone and granitic basement. In fact, the sandstone-granite fault at Illkirch could influence the nature and the amount of the clogging differently than the intra-granite faults, such as those in Soultz-sous-Forêts and Rittershoffen. Additionally, the km-length vertical offset of the Eschau fault could explain the mineral clogging due to the high fluid/rock ratio, as well as the smearing induced by the clayey Permian layers.

5.2. *Which is the most permeable reservoir?*

The dataset studied in this paper reveals that the initial permeability is very localized and intimately linked to the fractures in both the sediments and granite.

The most permeable reservoir in the URG is the top of the granitic basement (Vidal and Genter, 2018). The highest fracture density and thickest fractures are located in the first 500–1000 m of the hidden granitic basement (Figs. 7 and 9). By excluding the bias of the tool resolution, the highest fracture density values are observed in GIL-1 and GPK-2 (1.6 and 1.2 frac/m, respectively). Even if GIL-1 has a higher fracture density than GRT-2 (0.79 frac/m), the natural permeability of GIL-1 is lower. GRT-2 also presents a lower fracture thickness density and a lower fracture thickness average compared to GIL-1. For example, the trajectory of the deviated GRT-2 well intersects the Rittershoffen fault zone over a length of more than 400 m and provides the best hydraulic productivity index due to connection between the well and the fracture network in the near-well field (Baujard et al., 2017). Indeed, this fracture network intersected (NNW-SSE) is colinear to the local fault roughly N–S. The fracture distribution in GRT-2 is quite regular, with a negative exponential law (Fig. 8d) but with a high concentration of localized permeable fractures at the intersection of the Rittershoffen fault zone extending throughout the entire granitic part of the well (Fig. 7). These observations tend to show that more than the fracture density, it is the connection of the fractures intersected by a larger fault zone that contributes to the natural permeability (Neuman, 2008).

At Soultz-sous-Forêts, the local Soultz fault oriented N020°E was intersected in the Triassic formations and revealed natural permeability (Traineau et al., 1992; Vidal et al., 2015). However, the permeable fracture network intersected in the granite, which is oriented NNW-SSE, is probably more connected to a series of highly connected local-scale faults, with the largest one being oriented N145°E (Sausse et al., 2010). Between the top basement and 5000 m depth, several depth sections with variable fracture densities are observed (Fig. 7a). The hydraulic studies showed that there are 3 superimposed reservoirs in the granite: the upper one in the first 850 m of the granite (1400–2200 m MD), the middle one between 1550 and 2450 m (3000–3900 m MD) and the deepest one between 3650 and 3950 m (4000–5400 m MD) (Dezayes et al., 2010; Schill et al., 2017). In the first 500 m and from 1500 to 2000 m in the granite, the fracture density is higher (0.4–1.2 and 0.4–0.8 frac/m respectively) corresponding to the upper and middle reservoirs. These 3 reservoirs are also reflected by the cumulative fracture thicknesses along the depth (Fig. 7). Hence, in GPK-3, we observe 3 plateaus, as follows: from 1530 to 2040 m MD, corresponding to the upper reservoir; from 3000 to 3200 m MD, corresponding to the top of the middle reservoir; and from 4350 to 5000 m MD, corresponding to the deepest reservoir (Fig. 9). The fracture spacings distribution in the EPS-1 well indicates a quite clustered spatial fracture network distribution in the upper reservoir, which could promote fracture connectivity and then higher permeability (Fig. 8). The most permeable FZ is located in the upper reservoir, i.e., in the GPK-2 well at 2120 m MD, which showed total mud losses during drilling operations (Sausse et al., 2010). Its

injectivity index is 20 L/s/bar, which is three orders of magnitude higher than in the middle and deepest reservoirs (Schill et al., 2017). For example, the highest hydraulic yield before stimulation in the deepest reservoir observed in GPK-3 corresponds to the path of a local fault, which bears 70% of the flow (Dezayes et al., 2010).

Indeed, at Illkirch, the local Eschau fault oriented N30°E at the borehole scale was intersected at the interface of the sedimentary cover and the granitic basement, but the permeable fractures are oriented NNW-SSE, which is quite different from the local fault orientation. The local fault was probably intersected in GIL-1 but does not present permeability evidence at the borehole scale, which may be due to the intense mineral clogging linked to paleo-circulations around this fault. The permeability seems more linked to the intra-granite fractures in the deepest part of the well (>3100 m MD), thus far away from this main faulted interface (2894 m MD). The permeability is lower in GIL-1 than in GRT-2, which is probably because the local normal fault zone intersected in GRT-2 exploits a first-order permeability that responds locally and rapidly. The Illkirch well is probably connected to a wide and regular network of small-scale fractures affecting the whole granitic batholith and corresponding to a distributed permeability. By considering a second geothermal well at the Illkirch site close to the first GIL-1 well, as there is no local intra-granite fault, the goal would be to maximize the connection between the intra-granite fractures and this future targeted well. As they are always the same inherited NNW-SSW to N–S fractures that are encountered in the granitic basement, the well trajectory should favour a W-E direction with an inclination normal to the nearly vertical fractures planes, which means inclinations between 20 and 40°.

The geothermal experience in the Central URG reveals that the most permeable reservoir is located in the first 500–1000 m (TVD) of the granitic basement, which is characterized by high fracture densities and high fracture thicknesses. The trajectory of future wells should be optimized towards local intra-granite fault zones with deep dips. The inclination of the well should allow the intersection on the permeable fault zone over a greater length to maximize the connection between the well and the fracture network. The reservoir should present significant but not too important traces of fluid/rock interactions, such as secondary clay minerals and geodic quartz. Inherited fault zones from the Variscan period, probably channelize the natural hydrothermal circulations and are ideal structural targets, particularly when they are intra-granite. The trajectory tangent to the fault zone, such as in the GRT-2 well, allowed a hydrothermal well to be obtained that did not need any stimulations and that produces 3.5 L/s/bar (Baujard et al., 2017).

6. Conclusion

In geothermal reservoirs of the Central URG, we have analysed the structural characteristics of fractured networks based on borehole images and extensive coring from 8 geothermal wells at 3 sites: Soultz-sous-Forêts, Rittershoffen and Illkirch.

- In the three sites, the fractures follow the Rhenish direction (NNE-SSW) in the Buntsandstein sandstones and Muschelkalk limestones. In the granite, fractures strike NNW-SSE to N–S following the late-Variscan inherited directions.
- Few permeable fractures were observed in the Triassic sediments. At Illkirch, the faulted interface between sandstone and granite is tight and does not present interesting permeability. In the granite, the permeable fractures intersected by the Soultz-sous-Forêts and Rittershoffen wells present a conjugate set striking N–S, close to the Illkirch striking direction which is NNW-SSE. For all sites, all the permeable fractures are steeply dipping (85°E and W) and striking sub-parallelly to the maximum horizontal stress direction±10°.
- In the granitic basement, the fracture spacings distribution is governed by power laws and negative exponential laws, reflecting a clustered organization of the fractures. Hence, these closely spaced fractures define connected FZs, which are potential fluid pathways.
- In the three sites, the fracture density and the fracture thickness are the greatest in the first 500–1000 m of the basement; this depth section is spatially correlated with the most permeable reservoirs. However, high fracture thickness and high fracture density are not systematically related to high permeabilities. In fact, the permeability depends mainly of the connectivity of the fractures and requires a good equilibrium between the dissolution and precipitation processes to preserve the natural fluid channels.

The structural inheritance predisposes the organization of fractures in the reservoir and governs the hydrothermal inheritance. The permeability is mainly controlled by nearly vertical fracture networks intersecting both the Triassic sandstone and the crystalline Palaeozoic basement. In the Central URG, the most promising target is to intersect and run tangent to highly dipping local normal faults intra-top granite.

CRediT authorship contribution statement

Carole Glaas: Conceptualization, Methodology, Validation, Investigation, Data curation, Writing – review & editing, Formal analysis, Writing – original draft, Visualization. **Jeanne Vidal:** Conceptualization, Methodology, Validation, Investigation, Data curation, Writing – review & editing. **Albert Genter:** Conceptualization, Methodology, Validation, Investigation, Data curation, Writing – review & editing, Resources, Supervision, Project administration, Funding acquisition.

Declaration of competing interest

The authors declare that they have no known competing financial interests or personal relationships that could have appeared to influence the work reported in this paper.

Acknowledgements

This manuscript was prepared as a contribution to the PhD thesis (University of Strasbourg) of Carole Glaas which is cofounded by ES-Géothermie and ANRT (French Agency for Research and Technology). The authors acknowledge the EGS Alsace project funded by ADEME (French Agency for Environment), as well as the Cantare Alsace project funded by ANR Programme under the grant agreement ANR-15-CE06-0014. The authors also acknowledge GEIE EMC, ECOGI, and ESIG for providing the Soultz-sous-Forêts, Rittershoffen and Illkirch fracture datasets.

Appendix A. Supplementary data

Supplementary data to this article can be found online at https://doi.org/10.1016/j.jsg.2021.104370.

Role of the funding source

This contribution received funding from EGS Alsace project funded by ADEME (French Agency for Environment), as well as from the Cantare Alsace project funded by ANR Programme under the grant agreement ANR-15-CE06-0014. The public funding sources has no involvement in the conduct of the research and/or preparation of the article.

Data availability

Data of the Soultz-sous-Forêts wells can be requested at guichet.H@brgm.fr. Data of the Rittershoffen wells belong to ECOGI. Data of the Illkirch well belong to ESIG. Please contact ES-Géothermie for data requests at geothermie@es.fr.

References

Aichholzer, C., 2019. Le log complet de la stratigraphie de la zone rhénane ainsi que les modalités stratigraphies, sédimentaires et structurales de la transition "socle-couverture". Application à la géothermie profonde. PhD, Université de Strasbourg, France.

Aichholzer, C., Duringer, Ph, Genter, A., 2019. Detailed descriptions of the lower-middle Triassic and Permian formations using cores and gamma-rays from the EPS-1 exploration geothermal borehole (Soultz-sous-Forêts, Upper Rhine Graben, France). Geoth. Energy 7, 34. https://doi.org/10.1186/s40517-019-0148-1.

Altherr, R., Henes-Klaiber, U., Hegner, E., Langer, C., 1999. Plutonism in the Variscan Odenwald (Germany): from subduction to collision. Int. J. Earth Sci. 422–443.

Altherr, R., Holl, A., Hegner, E., Langer, C., Kreuzer, H., 2000. High-potassium, calc-alkaline I-type plutonism in the European Variscides: northern Vosges (France) and northern Schwarzwald (Germany). Lithos 50, 51–73.

Baillieux, P., Schill, E., Edel, J.-B., Mauri, G., 2013. Localization of temperature anomalies in the Upper Rhine Graben: insights from geophysics and neotectonic activity. Int. Geol. Rev. 55, 1744–1762. https://doi.org/10.1080/00206814.2013.794914.

Baria, R., Baumgaertner, J., Teza, D., Bennett, T., Glass, H., Jupe, A., 2016. Development of geothermal technology to address the climate change issue in the densely populated areas of the world. In: European Geothermal Congress 2016. Presented at the European Geothermal Congress 2016, Strasbourg, France, vol. 8.

Barton, C.A., Zoback, M.D., Moos, D., 1995. Fluid flow along potentially active faults in crystalline rock. Geology 23, 683–686. https://doi.org/10.1130/0091-7613(1995)023<0683:FFAPAF>2.3.CO;2.

Bauer, J.F., Meier, S., Philipp, S.L., 2015. Architecture, fracture system, mechanical properties and permeability structure of a fault zone in Lower Triassic sandstone, Upper Rhine Graben. Tectonophysics 132–145. https://doi.org/10.1016/j.tecto.2015.02.014.

Baujard, C., Genter, A., Dalmais, E., Maurer, V., Hehn, R., Rosillette, R., Vidal, J., Schmittbuhl, J., 2017. Hydrothermal characterization of wells GRT-1 and GRT-2 in Rittershoffen, France: implications on the understanding of natural flow systems in the Rhine Graben. Geothermics 65, 255–268. https://doi.org/10.1016/j.geothermics.2016.11.001.

Baumgärtner, D.J., Lersch, 2013. Geothermie 2.0 the geothermal power plant Insheim. EGR, 21.

Bergerat, F., 1985. Déformations cassantes et champs de contrainte tertiaires dans la plate-forme européenne. PhD, Paris VI.

Bertrand, L., Gavazzi, B., Mercier de Lépinay, J., Diraison, M., Géraud, Y., Munschy, M., 2020. On the Use of aeromagnetism for geological interpretation: 2. A case study on structural and lithological features in the northern Vosges. J. Geophys. Res.: Solid Earth 125. https://doi.org/10.1029/2019JB017688.

Bossennec, C., Geraud, Y., Bertrand, L., Mattioni, L., Moretti, I., 2020. Insights on fluid sources and pathways in geothermal sandstone reservoir by structural and geochemical characterization of fractures infills. In: Presented at the World Geothermal Congress 2020, Reykjavik, vol. 12.

Brogi, A., 2008. Fault zone architecture and permeability features in siliceous sedimentary rocks: insights from the Rapolano geothermal area (Northern Apennines, Italy). J. Struct. Geol. 30, 237–256. https://doi.org/10.1016/j.jsg.2007.10.004.

Burg, J.P., Matte, Ph, Leyreloup, A., Marchand, J., 1984. Inverted metamorphic zonation and large-scale thrusting in the Variscan Belt: an example in the French Massif Central. Geol. Soc. London, Special Publications 14, 47–61. https://doi.org/10.1144/GSL.SP.1984.014.01.05.

Caine, J.S., Evans, J.P., Forster, C.B., 1996. Fault zone architecture and permeability structure. Geology 24, 1025–1028. https://doi.org/10.1130/0091-7613(1996)024<1025:FZAAPS>2.3.CO;2.

Clauer, N., Liewig, N., Ledesert, B., Zwingmann, H., 2008. Thermal history of Triassic sandstones from the Vosges Mountains-Rhine Graben rifting area, NE France, based on K-Ar illite dating. Clay Miner. 43, 363–379. https://doi.org/10.1180/claymin.2008.043.3.03.

Cocherie, A., Guerrot, C., Fanning, C.M., Genter, A., 2004. Datation U–Pb des deux faciès du granite de Soultz (Fossé rhénan, France). Compt. Rendus Geosci. 336, 775–787pp. https://doi.org/10.1016/j.crte.2004.01.009.

Crain, E.R., 1998. The Log Analysis Handbook. Petroleum Engineering, United States.

Curewitz, D., Karson, J.A., 1997. Structural settings of hydrothermal outflow: fracture permeability maintained by fault propagation and interaction. J. Volcanol. Geoth. Res. 149–168.

Dezayes, C., Genter, A., Valley, B., 2010. Structure of the low permeable naturally fractured geothermal reservoir at Soultz. C. R. Geoscience 342, 517–530. https://doi.org/10.1016/j.crte.2009.10.002.

Dezayes, C., Lerouge, C., 2019. Reconstructing paleofluid circulation at the Hercynian basement/Mesozoic sedimentary cover interface in the Upper Rhine Graben. Geofluids 2019, 1–30. https://doi.org/10.1155/2019/4849860.

Dèzes, P., Schmid, S.M., Ziegler, P.A., 2004. Evolution of the European Cenozoic rift system: interaction of the alpine and pyrenean orogens with their foreland lithosphere. Tectonophysics 389, 1–33. https://doi.org/10.1016/j.tecto.2004.06.011.

Doebl, F., 1967. The tertiary and pleistocene sediments of the northern and central part of the upper Rhinegraben. Abh. Geol. Landesans., The Rhinegraben Progress Report 1967 6, 48–54.

Edel, J.-B., Schulmann, K., 2009. Geophysical constraints and model of the "Saxothuringian and Rhenohercynian subduction - magmatic arc system" in NE France and SW Germany. Bull. Soc. Geol. Fr. 6, 545–558.

Edel, J.-B., Schulmann, K., Rotstein, Y., 2007. The Variscan tectonic inheritance of the upper Rhine graben: evidence of reactivations in the lias, late Eocene–Oligocene up to the recent. Int. J. Earth Sci. 2, 305–325. https://doi.org/10.1007/s00531-006-0092-8.

Edel, J.-B., Whitechurch, H., Diraison, M., 2006. Seismicity wedge beneath the upper Rhine graben due to backwards alpine push? Tectonophysics 428, 49–64. https://doi.org/10.1016/j.tecto.2006.08.009.

Evans, K.F., Genter, A., Sausse, J., 2005. Permeability creation and damage due to massive fluid injections into granite at 3.5 km at Soultz: 1. Borehole observations. J. Geophys. Res.: Solid Earth 110. https://doi.org/10.1029/2004JB003168.

Evans, K.F., Zappone, A., Kraft, T., Deichmann, N., Moia, F., 2012. A survey of the induced seismic responses to fluid injection in geothermal and CO2 reservoirs in Europe. Geothermics 41, 30–54. https://doi.org/10.1016/j.geothermics.2011.08.002.

Faulds, J.E., Hinz, N.H., Coolbaugh, M.F., Cashman, P.H., Kratt, C., Dering, G., Edwards, J., Mayhew, B., McLahan, H., 2011. Assessment of favorable structural settings of geothermal systems in the Great Basin, western USA. In: Presented at the Geothermal Resources Council Transactions, pp. 777–784.

Faulkner, D.R., Jackson, C.A.L., Lunn, R.J., Schlische, R.W., Shipton, Z.K., Wibberley, C.A.J., Withjack, M.O., 2010. A review of recent developments concerning the structure, mechanics and fluid flow properties of fault zones. J. Struct. Geol. 32, 1557–1575. https://doi.org/10.1016/j.jsg.2010.06.009.

Genter, A., Castaing, C., Dezayes, C., Tenzer, H., Traineau, H., Villemin, T., 1997. Comparative analysis of direct (core) and indirect (borehole imaging tools) collection of fracture data in Hot Dry Rock Soultz reservoir (France). J. Geophys. Res. 102 (15), 419-15,431.

Genter, A., Martin, P., Montaggioni, P., 1992. Application of FMS and BHTV tools for evaluation of natural fractures in the Soultz geothermal borehole GPK-1. Geothermal energy in Europe - the Soultz hot dry rock project. Sur GR j'ai Que 69–82.

Genter, A., Traineau, H., 1996. Analysis of macroscopic fractures in granite in the HDR geothermal well EPS-l, Soultz-sous-Forêts, France. J. Volcanol. Geoth. Res. 121–141.

Genter, A., Traineau, H., Ledésert, B., Bourgine, B., Gentier, S., 2000. Over 10 Years of Geological Investigations within the HDR Soultz Project, France. Presented at the World Geothermal Congress. Kyushu, Japan, pp. 3707–3712.

Gentier, S., Rachez, X., Dezayes, C., Blaisonneau, A., Genter, A., 2005. How to understand the effect of the hydraulic stimulation in terms of hydro-mechanical behavior at Soultz-sous-Forêts (France). GRC Trans. 29.

Gillespie, P.A., Walsh, J.J., Watterson, J., Bonson, C.G., Manzocchi, T., 2001. Scaling relationships of joint and vein arrays from the Burren, Co. Clare, Ireland. J. Struct. Geol. 183–201.

Glaas, C., Genter, A., Girard, J.-F., Patrier, P., Vidal, J., 2018. Permeability approach in deep fractured reservoirs of the Upper Rhine Graben. Hydrothermal Alteration (Clays) and Electrical Logs Analyze in the Geothermal Wells of Alsace (France). 9th European Geothermal PhD Days. ETH, Zürich.

Glaas, C., Patrier, P., Vidal, J., Beaufort, D., Girard, J.F., Genter, A., 2021. Hydrothermal alteration in the new deep geothermal well GIL-1 (Strasbourg area, France). In: Presented at the World Geothermal Congress 2020, Reykjavik, vol. 11.

Gudmundsson, A., Fjeldskaar, I., Brenner, L.S., 2002. Propagation pathways and fluid transport of hydrofractures in jointed and layered rocks in geothermal fields. J. Volcanol. Geoth. Res. 116, 257–278. https://doi.org/10.1016/S0377-0273(02)00225-1.

Häring, M.O., Schanz, U., Ladner, F., Dyer, B.C., 2008. Characterisation of the Basel 1 enhanced geothermal system. Geothermics 37, 469–495. https://doi.org/10.1016/j.geothermics.2008.06.002.

Hehn, R., Genter, A., Vidal, J., Baujard, C., 2016. Stress field rotation in the EGS well GRT-1 (Rittershoffen, France). In: Presented at the European Geothermal Congress, Strasbourg.

Henriksen, A., 2001. Fracture interpretation based on electrical and acoustic borehole logs. No. BRGM/RP-50835-FR. BRGM Orléans, France.

Housse, B.A., 1984. Reconnaissance du potentiel géothermique du Buntsandstein à Strasbourg-Cronenbourg. Geothermie Actual. 36–41.

Illies, J.H., 1972. The Rhine graben rift system-plate tectonics and transform faulting. Geophys. Surv. 1, 27–60. https://doi.org/10.1007/BF01449550.

Illies, J.H., Greiner, G., 1979. Holocene movements and state of stress in the Rhinegraben rift system. Tectonophysics 52, 349–359.

Jung, R., Schindler, M., Nami, P., Tischner, T., 2010. Determination of flow exits in the Soultz borehole GPK2 by using the brine displacement method. Compt. Rendus Geosci. 342, 636–643. https://doi.org/10.1016/j.crte.2009.06.002.

Kappelmeyer, O., 1991. European HDR project at Soultz-sous-Forêts general presentation. Geotherm. Sci. Technol. 263–289.

Lagarde, J.-L., Capdevila, R., Fourcade, S., 1992. Granites et collision continentale : l'exemple des granitoïdes carbonifères dans la chaîne hercynienne ouest-européenne. Bull. Soc. Geol. Fr. 163, 597–610.

Ledésert, B., Berger, G., Meunier, A., Genter, A., Bouchet, A., 1999. Diagenetic-type reactions related to hydrothermal alteration in the Soultz-sous-Forets Granite, France. Eur. J. Mineral 11, 731–741.

Michon, L., Van Balen, R.T., Merle, O., Pagnier, H., 2003. The cenozoic evolution of the roer valley Rift System integrated at a European scale. Tectonophysics 367, 101–126. https://doi.org/10.1016/S0040-1951(03)00132-X.

Mitchell, T.M., Faulkner, D.R., 2012. Towards quantifying the matrix permeability of fault damage zones in low porosity rocks. Earth Planet Sci. Lett. 339 (340), 24–31. https://doi.org/10.1016/j.epsl.2012.05.014.

Mouchot, J., Ravier, G., Seibel, O., Pratiwi, A., 2019. Deep geothermal plants operation in upper Rhine graben: lessons learned. In: European Geothermal Congress 2019. Presented at the European Geothermal Congress 2019, Den Haag, The Netherlands, vol. 8.

Neuman, S.P., 2008. Multiscale relationships between fracture length, aperture, density and permeability. Geophys. Res. Lett. 35, L22402. https://doi.org/10.1029/2008GL035622.

Odling, N.E., Gillespie, P., Bourgine, B., Castaing, C., Chiles, J.-P., Christensen, N.P., Fillion, E., Genter, A., Olsen, C., Thrane, L., Trice, R., Aarseth, E., Walsh, J.J., Watterson, J., 1999. Variations in fracture system geometry and their implications for fluid flow in fractured hydrocarbon reservoirs. Petrol. Geosci. 5, 373–384.

Pribnow, D., Schellschmidt, R., 2000. Thermal tracking of upper crustal fluid flow in the Rhine graben. Geophys. Res. Lett. 27, 1957–1960. https://doi.org/10.1029/2000GL008494.

Reinecker, J., Hochschild, T., Kraml, M., Löschan, G., Kreuter, H., 2019. Experiences and challenges in geothermal exploration in the upper Rhine graben. In: Presented at the European Geothermal Congress, 8.

Richard, A., Maurer, V., Edel, J.-B., Genter, A., Baujard, C., Dalmais, E., 2016. Towards Targeting Geothermal Reservoir: Exploration Program for a New EGS Project in Urban Context in Alsace. European Geothermal Congress, Strasbourg, France.

Sausse, J., Dezayes, C., Dorbath, L., Genter, A., Place, J., 2010. 3D model of fracture zones at Soultz-sous-Forêts based on geological data, image logs, induced microseismicity and vertical seismic profiles. Compt. Rendus Geosci. 342, 531–545. https://doi.org/10.1016/j.crte.2010.01.011.

Sausse, J., Genter, A., 2005. Types of permeable fractures in granite. Geological Society, London, Special Publications 240, 1–14. https://doi.org/10.1144/GSL.SP.2005.240.01.01.

Sausse, J., Genter, A., Leroy, J.L., 1998. Description et quantification des altérations filoniennes : paléoécoulements fluides dans le granite de Soultz-sous-Forêts (Bas-Rhin, France). Bulletin de La Societe Geologique de France 28.

Schellschmidt, R., Clauser, C., 1996. The thermal regime of the upper Rhine graben and the anomaly at Soultz. Z. Angew. Geol. 42, 40–44.

Schill, E., Genter, A., Cuenot, N., Kohl, T., 2017. Hydraulic performance history at the Soultz EGS reservoirs from stimulation and long-term circulation tests, 70, pp. 110–124. https://doi.org/10.1016/j.geothermics.2017.06.003.

Schlumberger, 1993. Schlumberger wireline and testing. Houston, Texas 77252-2175.

Schumacher, M.E., 2002. Upper Rhine Graben: Role of preexisting structures during rift evolution. Tectonics 21. https://doi.org/10.1029/2001TC900022, 6-1-6–17.

Serra, O., Serra, L., 2000. In: Diagraphies, Acquisition et applications. Serralog.

Stussi, J.-M., Cheilletz, A., Royer, J.-J., Chèvremont, P., Féraud, G., 2002. The hidden monzogranite of Soultz-sous-Forêts (Rhine Graben, France). Mineralogy, petrology and genesis. Géologie de La France 45–64.

Traineau, H., Genter, A., Cautru, J.-P., Fabriol, H., Chèvremont, Ph, 1992. Petrography of the granite massif from drill cutting analysis and well log interpretation in the geothermal HDR borehole GPK-1 (Soultz, Alsace, France). In: Geothermal Energy in Europe - the Soultz Hot Dry Rock Project. Bresee, James C., Montreux, Switzerland, pp. 1–29.

Valley, B., Evans, K.F., 2007. Stress state at Soultz-sous-Forêts to 5 Km depth from wellbore Failure and hydraulic observations, 10.

Vidal, J., Genter, A., 2018. Overview of naturally permeable fractured reservoirs in the central and southern Upper Rhine Graben: insights from geothermal wells. Geothermics 74, 57–73. https://doi.org/10.1016/j.geothermics.2018.02.003.

Vidal, J., Genter, A., Chopin, F., 2017. Permeable fracture zones in the hard rocks of the geothermal reservoir at Rittershoffen, France. J. Geophys. Res.: Solid Earth 122, 4864–4887. https://doi.org/10.1002/2017JB014331.

Vidal, J., Genter, A., Schmittbuhl, J., 2016. Pre- and post-stimulation characterization of geothermal well GRT-1, Rittershoffen, France: insights from acoustic image logs of hard fractured rock. Geophys. J. Int. 845–860.

Vidal, J., Genter, A., Schmittbuhl, J., 2015. How do permeable fractures in the Triassic sediments of Northern Alsace characterize the top of hydrothermal convective cells? Evidence from Soultz geothermal boreholes (France). Geoth. Energy 3, 8. https://doi.org/10.1186/s40517-015-0026-4.

Vidal, J., Hehn, R., Glaas, C., Genter, A., 2019. How can temperature logs help identify permeable fractures and define a conceptual model of fluid circulation? An example from deep geothermal wells in the Upper Rhine Graben. Geofluids 14. https://doi.org/10.1155/2019/3978364.

Vidal, J., Patrier, P., Genter, A., Beaufort, D., Dezayes, C., Glaas, C., Lerouge, C., Sanjuan, B., 2018. Clay minerals related to the circulation of geothermal fluids in boreholes at Rittershoffen (Alsace, France). J. Volcanol. Geoth. Res. 349, 192–204. https://doi.org/10.1016/j.jvolgeores.2017.10.019.

Villemin, T., Bergerat, F., 1987. L'évolution structurale du fossé rhénan au cours du Cénozoïque : un bilan de la déformation et des effets thermiques de l'extension. Bull. Soc. Géol. France 8, 245–255.

Zemaneck, J., Glen, E.E.J., Norton, L.J., Cardwell, R.L., 1970. Formation evaluation by inspection with the borehole televiewer. Geophysics 2, 254–269.

Ziegler, P.A., 1992. European Cenozoic rift system. Case history studies on rifts: European and Asian. Tectonophysics 91, 11.

Ziegler, P.A., Schumacher, M.E., Dèzes, P., Van Wees, J.-D., Cloetingh, S., 2006. Post-variscan evolution of the lithosphere in the area of the European Cenozoic rift system. Geol. Soc. , London, Memoirs 32, 97–112.